Growth of oriented orthotropic structures with reaction/diffusion

David-Henri Garnier, Martin-Pierre Schmidt, Damien Rohmer

Growth of Oriented Orthotropic Structures with Reaction/Diffusion

AUTHOR'S VERSION

Published in *Structural and Multidisciplinary Optimization* on November 5th 2022
DOI : 10.1007/s00158-022-03395-7

-

David-Henri Garnier[1], Martin-Pierre Schmidt[2], Damien Rohmer[1]
[1] LIX, Ecole Polytechnique, CNRS, IP Paris, France
[2] LMI, Normandie Univ., INSA Rouen, 76000 Rouen, France

-

Corresponding author: david-henri.garnier@polytechnique.edu
Contributing authors: martinpierre.schmidt@insa-rouen.fr, damien.rohmer@polytechnique.edu

November 7, 2022

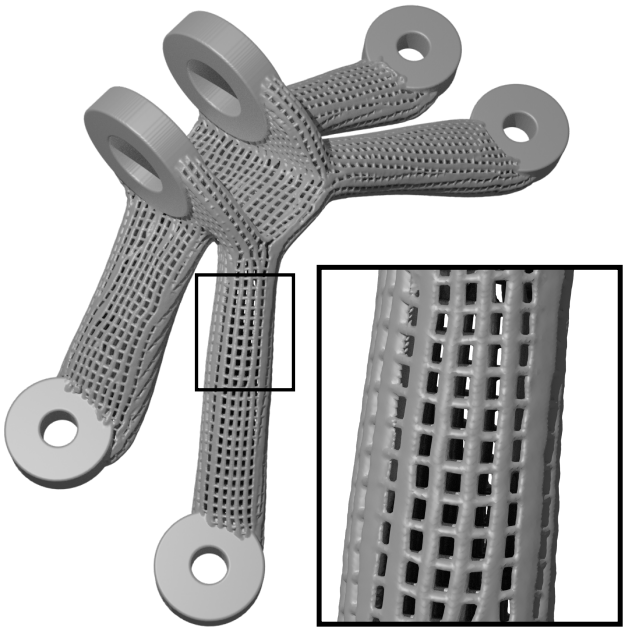

Figure 1: Lattice *GE Bracket* grown by our method on a mesh of $308 \times 518 \times 833$ regular hexahedra.

Abstract

Lattice structures can present advantageous mechanical properties while remaining remarkably lightweight. Precise lattice design can however be tricky to set up with classical 3D modeling methods as it involves very fine details. Interestingly, natural porous structures can present such lattice-like or membrane-like features which motivates to seek for more bio-inspired approaches to microstructure design. In this paper we present a novel method to grow lattice-like and membrane-like structures within an arbitrary shape and aligned along an oriented field. Our method relies on the use of a dedicated anisotropic Reaction-Diffusion system guided by an orthotropic diffusion tensor field. Assuming for instance the diffusion tensor to be related to the stress analysis of a given shape allows to generate emerging stripes patterns aligned along each one of the principal stress directions independently. A globally coherent mechanical model conforming to the initial shape boundary and infilled with oriented microstructures can therefore be synthesized. Further, we demonstrate the capability of this approach to handle other types of oriented fields such as obtained through optimization of material directions in scenarios with multiple load-cases. Our approach relies on spatially and temporally local operations allowing for efficient parallelization. This permits user-interaction and automated adaptation of the design, even for fine meshes over large volumes. For instance, a designer can locally erase or "draw" over the structure and let it regrow and adapt as well as enforce regions to be deliberately full or empty. The proposed approach yields smooth and conformal oriented anisotropic geometrical patterns. This is related to recent effort in the *Structural Optimization* community on the topic of optimized oriented infills and microstructure de-homogenization. One of the resulting designs is validated by means of a full scale general nonlinear analysis showcasing the advantageous properties of oriented microstructures for stability and robustness to buckling.

Keywords: Reaction-Diffusion, Anisotropy, Topology Optimization, Additive Manufacturing, Micro-structures.

1 Introduction

Recent advances in Additive Manufacturing and 3D Printing allows for high shape complexity that leads to seek for new lightweight designs. Hence there has been a growing interest in design of optimized multi-scale structures recently reviewed by Wu et al. (2021a). Simplified methods to generate such structures often rely on infilling 3D shapes with regular microstructures.

In such case the infill pattern presents typically anisotropic mechanical properties (e.g. a regular hollowed cubic cell is stiffer along its axes than along other directions) which can be desirable to enhance the mechanical performance of the global shape. This approach has a major shortcoming in that the cells are aligned with the model axis directions and not with the load paths, making for poor structural performance. In addition the microstructure has to be enclosed by a load-bearing shell, as the cells cannot mesh conformally to an outer boundary. In short, this limits the solution space and thus the structure properties.

Let us consider the case of a design region undergoing a single-load case. In such case, and as long as long as the geometrical constraints make this possible (Podersen (1998); Pedersen (2000)), the stress does not exhibit local concentration within the shape, and it is known that a stiffness-optimal structure can be made by aligning the local orientation of an orthotropic material properties with the principal stresses (Pedersen (1989)). In our case, we will make it from a hexahedral grid – that we designate as *lattice* – with edges locally aligned along the principal stress directions. However, computing a continuous lattice that locally adapts to the stress direction for arbitrary design boundaries is a challenging problem. Our growth-based approach is able to generate such generic oriented-lattice for a given design region and stress distribution, and is therefore able to generate a stiffness-optimized structure when the optimality-assumptions are met. But our method can further be extended to more general – although not necessarily optimal – cases where the shape exhibits local stress concentration while still providing coherent oriented microstructure locally mixed with solid material regions. In addition, the same framework can be used to generate oriented membranes instead trusses.

According to Jakob et al. (2015), meshing algorithms able to generate hexahedral-grid with spatially varying orientation divide into two major classes: local and global methods. The former are usually simpler and scalable but tend to introduce many singularities, i.e., points in the output mesh where the connectivity deviates from that of a regular lattice like T-junctions, and they do not usually support alignment of the output mesh with surface features (Lai et al. (2008)). The latter solve an optimization problem whose size depends on the mesh, increasing quality at the sacrifice of scalability (Kälberer et al. (2007); Bommes et al. (2009); Ebke et al. (2014)). Although our method relies on local computations, the structure is grown from a small seed thus leaving few topological defects in the final structure. It also makes it easy for the final shape to capture the surface features while still allowing fast editing by local modifications of the underlying tensor field. The *Structural Optimization* community already approached this problem in the context of microstructure de-homogenization. Assuming that our structure has been parameterized with multiple parameters so that their homogenized material properties have been optimized, the de-homogenization consists in reconstructing a manufacturable structure made of discrete elements. It could be noted that our generative approach can find application in the context of de-homogenization in order to build efficiently discrete elongated and oriented structures.

Some natural materials show remarkable mechanical performance based on this stress orientation property. Wood, for instance, presents a natural polar anisotropy provided by evolution, being most stiff along the grain than through its radial and circumferential directions (Wood (1960)). Hence the study of natural shape formation as well as morphogenesis gives interesting prospects for optimal design although few works attempt to inspire from morphogenesis in the field of structural optimization. Starting from this observation we propose to use a model of anisotropic Reaction/Diffusion because of its ability to grow patterns along a desired orientation.

In this paper, we describe a novel bio-inspired method to design conforming lattice-like and membrane-like structures. Our method divides into two major steps. The first step proposes to generate intermediate structures with patterns oriented by an underlying tensor field and limited by a prescribed 3D shape with a growing process. This growth phase is controlled by an anisotropic Reaction/Diffusion model which is able to leave some solid material in the areas where orientation singularities can occur. Each principal tensor direction of the tensor field is independently considered from the others and converted to an adapted diffusion field allowing to synthesize an oriented structure. The second step starts by applying some filter to the different structures to operate on the thickness of the oriented structures before combining them with Boolean operations in a similar way than Geoffroy-Donders et al. (2020). An overview of the method can be seen Fig. 2 which shows several steps of the growth of the final structure for a 4-legged stool scenario.

Our contributions are:

- A general method for designing field conformal lattice-like and membrane-like structures, compatible with the workflow of topology optimization
- A novel approach based on a classic Reaction/Diffusion model to design global structure using anisotropic growth of microstructures
- A new process to design structures which constitute a good trade-off between stiffness property and resistance to buckling despite not being directly an optimizer of these properties

The present article is organized as follows. We start by a review of the related work in section 2. Section 3 gives an overview of the method. In section 4 and 5 the two main steps of our method, the pattern growth and the structure compilation, are detailed. Results with analysis are discussed section 6.

2 Related work

Our work is among recent efforts on structural optimization for 3D printing and topology optimization of multi-scale structures which both became thriving fields in the past decade. Because it borrows from a morphogenesis process our approach also belongs to the cross field of bio-inspired design.

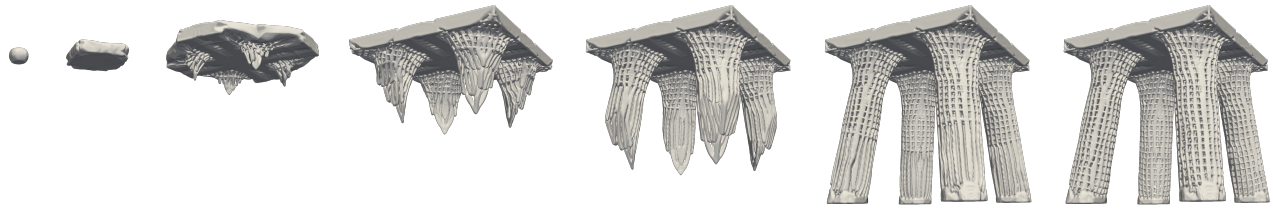

Figure 2: Growth steps for a 4-legged stool scenario with uniform downward loading on the top plate and zero displacement at the bottom of the 4 legs on a mesh of $295 \times 295 \times 295$ regular hexahedra.

2.1 Optimized design for Additive Manufacturing

Progresses in 3D printing gave a new dynamic to computational design (Alfaify et al. (2020)). Above all, structural optimization has become remarkably popular in the field (Liu et al. (2018b); Attene et al. (2018)). Common approaches relies on lightweight filling a predefined 3D shape using various infill such as honeycomb structures (Ahsan and Khoda (2021)), laminar structures (Stutz et al. (2022)), lattice (Dong et al. (2017)), Voronoï cells (Martínez et al. (2016); Lu et al. (2014)), bone-like porous structures (Wu et al. (2018)) or othotropic foam (Martínez et al. (2017)). Our work builds upon this design approach and proposes a method to infill a prescribed 3D shape with lattice-like material aligned with a desired local orientation while allowing specific areas to remain completely solid.

Because our approach results from a diffusion process, the structure smoothly meet the boundary surface of the input 3D shape regardless of the local orientation hence no additional treatment is required to obtain a conformal lattice structure (Brennan-Craddock (2011); Nguyen et al. (2012)) nor to rely on an outer shell (Clausen et al. (2015, 2016); Wu et al. (2017); Groen et al. (2019)). Furthermore the patterns generated by the model of Reaction/Diffusion are properly connected for well-chosen parameters specified in Sec. 4.4, avoiding any branching regularization operated by Tricard et al. (2020) or Elingaard et al. (2022).

Based on the principle that stress-aligned structure is best for stiffness improvement (Michell (1904); Pedersen (1989); Allaire and Kohn (1993)), Arora et al. (2019) proposed a parametric method to design Michell trusses destined to be 3D printed. However their method is based on a global parameterization which is computationally expensive, with a high sparsity purpose, which makes their approach more adapted to generate structures with few beams. Ours is more suitable for a large number of cells and also provides a filtering step allowing to link the thickness of the oriented patterns to their stress direction.

2.2 Homogenization-based Topology Optimization

Thanks to the theory of homogenization (Bensoussan et al. (1979)), able to describe the macroscale (homogenized) properties of periodic composite microstructures, it has been established that a class of sequential laminates, called the rank-N laminates, and composed of an infinity of spatially geometric patterns spanning multiple length scales, are necessary to achieve ultimate stiffness (Francfort and Murat (1986); Allaire and Aubry (1999)). The seminal paper by Bendsøe and Kikuchi (1988) then introduced an interpretation with a material model composed of infinitely small square cells with rectangular holes and showed that near-optimal structures could be generated by optimizing the lengths of the rectangle as well as the orientation of the cells.

However, because of manufacturing constraints at the time, mono-scale approaches such as the SIMP method (Solid Isotropic Material with Penalization) were brought in, optimizing the distribution of a homogeneous isotropic material (Bendsøe (1989); Bendsøe and Sigmund (1999)) and convenient to implement (Sigmund (2001); Andreassen et al. (2011)). Lastly, the emergence of 3D printing technologies allowed to actually manufacture objects designed with such method but also gave a new dynamic to the area of research of optimized multi-scale structures.

According to Wu et al. (2021a) two main strategies can be adopted to design multi-scale structures with topology optimization. The first approach consists in performing a full-scale topology optimization on a high resolution grid to let multi-scale features appear naturally (Liu et al. (2018a)). Such method can be combined with the enforcement of porosity using the now widely known local volume constraints (Wu et al. (2018)) and further controlled with varying fields (Schmidt et al. (2019)). The second strategy, referred to as multi-scale approach, assumes a separation of the different length scales. For instance a common approach uses parameterized unit-cells with multiple parameters (including rotation to approach rank-N laminate design) and numerically optimizes these homogenized material properties. From this optimization, reconstructing a global connected and manufacturable structure is called the de-homogenization process. Even when restricted to periodic microstructures, this constitutes one challenging issue, especially because the stress field has a rotational symmetry of π. The most common methods which has been developed relies on the deformation of a periodic grid by a diffeomorphism with a cosine wave to project the microstructures (Pantz and Trabelsi (2008); Groen and Sigmund (2018); Allaire et al. (2019)). Not only that these methods should treat well the singularities caused by the stress field (Stutz et al. (2020)), their extensions to 3D bring other issues given that the principal stress directions are not well-ordered in 3D, requiring additional regularization steps (Geoffroy-Donders et al. (2020); Groen et al. (2020)). A different approach proposed by Wu et al. (2021b) consists to de-homogenizing a structure by finding a lattice structure whose edges are locally aligned with the optimized directions, inspired by field-aligned meshing from the *Computer Graphics* com-

munity (Jakob et al. (2015); Gao et al. (2017)).

Our method uses the properties of the anisotropic diffusion to grow microstructures aligned along a tensor field. In this way we avoid the problem caused by the rotational symmetry of π since the oriented growth happens on the two sides of a same direction. We show in the Results section that our approach can be employed as a de-homogenization method, in place of Elingaard et al. (2022) process, and give comparable results for rank-2 laminates.

2.3 Bio-Inspired Modeling

Multi-scale structures are prevalent in nature and can be found in various vegetals and animal bodies (Lakes (1993); Fratzl and Weinkamer (2007)). While their underlying processes of conception are not always understood, they generally offer remarkable mechanical properties. Lately this led to the emergence of a new field referred as *Bio-Inspired Modeling* or *Bio-Inspired Design*. The latter is commonly used in the context of structural design for Additive Manufacturing (Du Plessis et al. (2019); Podroužek et al. (2019); Zhang et al. (2020)). We restrict here to the field of 3D modeling otherwise terms such as *Morphogenetic Engineering* (Doursat et al. (2013)) or *Computer-Aided Biomimetics* (Kruiper et al. (2016, 2018)) can be employed for more general problem solving.

Compared to classical topology optimization, which can generate organic shapes using only mathematical optimization, *Bio-Inspired Modeling* finds its roots in the field of morphogenesis, and aims to use natural processes to produce optimized design. The interdisciplinary character of the field makes it difficult to regard it as a unique design process yet it is more a set of various approaches using distinct representations and occurring at different scales (Chaturvedi et al. (2005)). For instance, pattern formation can be described by numbers of approaches from biology, chemistry, physics, mathematics or computer graphics. In a seminal paper, Turing (1952) accounts pattern formation in nature to a Reaction/Diffusion mechanism. Because they are also easy to implement (Hutton et al. (2015)), various models of Reaction/Diffusion have been proposed in the literature (Murray (2001)) to describe the formation of specific patterns (FitzHugh (1961); Nagumo et al. (1962); Hagberg and Meron (1994); Kobayashi (1993); Kawasaki et al. (1997); Sanal (2014)). For our purpose we chose to use a model of Reaction/Diffusion introduced by Gray and Scott (1984) for their ability to generate oriented stripes whose direction can be controled through anisotropic diffusion.

Finally we should note that the Reaction/Diffusion equation has been used in level-set Topology Optimization techniques to directly drive the design (Yamada et al., 2010) (Choi et al., 2011) (Emmendoerfer Jr and Fancello, 2016), which is fairly different from what we present here. Only the recent work from Zhou et al. (2022) approaches what is presented here.

3 Method Overview

3.1 Outline

Let us consider a rectangular domain $\mathbf{\Omega}$, subset of $\mathbb{R}^2$ or $\mathbb{R}^3$, representing the domain of definition of the three following fields used as inputs of our method as illustrated in Fig 3-top. First the scalar field $\rho(\mathbf{x} \in \Omega) \in [0, 1]$, describes an initial notion of material density at each position in $\mathbf{\Omega}$. For a given isovalue $iso \in]0, 1[$, the domain implicitly defined by $\rho(\mathbf{x}) > iso$ corresponds to the general appearance of the 3D shape where the micro-structure should be synthesized, and will be designated as *infill space*. Second, a tensor field $\mathfrak{o}(\mathbf{x} \in \Omega)$ (for instance associated to the stress tensor), whose principal directions are considered to be the desired local orientation of the microstructures. Third, another scalar field $\Gamma(\mathbf{x} \in \Omega) \in [0, 1]$ called *infill map* used to indicate the local regions to infill preferentially with solid material instead of lattice microstructures.

Note that these inputs such as ρ and $\mathfrak{o}$ can typically be computed using topology optimization approaches, while we propose an automatic computation of Γ as described in Sec. 3.2. All inputs and intermediate field values are stored on a discretized grid, and we may pre-process these inputs in up-sampling if needed their values by interpolation to any grid resolution adapted to our expected lattice microstructure.

The output of our approach is also described as a scalar field $\mathcal{S}_{\rho,\mathfrak{o},\Gamma}(\mathbf{x} \in \Omega) \in [0, 1]$. The resulting shape surface is described as an isosurface of $\mathcal{S}$ which can be computed typically using the Marching Cubes or Dual Contouring algorithms when a triangular mesh is expected for visualization and manufacturing purpose. This surface represents a hybrid structure mostly filled with lattice aligned with both the tensor field directions and the boundary of the *infill space*. More precisely, at the boundary the lattice remains oriented according the tensor field while shaped by the outer shell.

The core of our algorithm lies in the two major steps $(\mathcal{RD})$ and $(\mathcal{B})$. Step $(\mathcal{RD})$ is the actual anisotropic Reaction/Diffusion process allowing to synthesize intermediate scalar fields with locally oriented patterns. We compute 2 (resp. 3) independent processes in 2D (resp. 3D), while considering for each of them one of the respective tensor direction to be the main diffusion direction. The anisotropic Reaction/Diffusion patterns have a lattice-like structure in 2D, and a membrane-like structure in 3D, and are restricted to grow in the regions specified by ρ as explained in Sec. 4. Once these intermediate fields are generated, the final structure is generated in step $(\mathcal{B})$. To this end, we first apply a filter $(\mathcal{F})$ on each of the intermediate fields in order to steepen the variations of the field as well as thickening or thinning the patterns depending on their directions. The output field $\mathcal{S}$ is finally obtained in combining the previous filtered fields using Boolean operations in order to generate a single structure from the individual oriented patterns. These last steps are described in Sec. 5.

3.2 Inputs

This section describes with more details the automatic computation we followed to generate the input fields ρ, $\mathfrak{o}$, Γ.

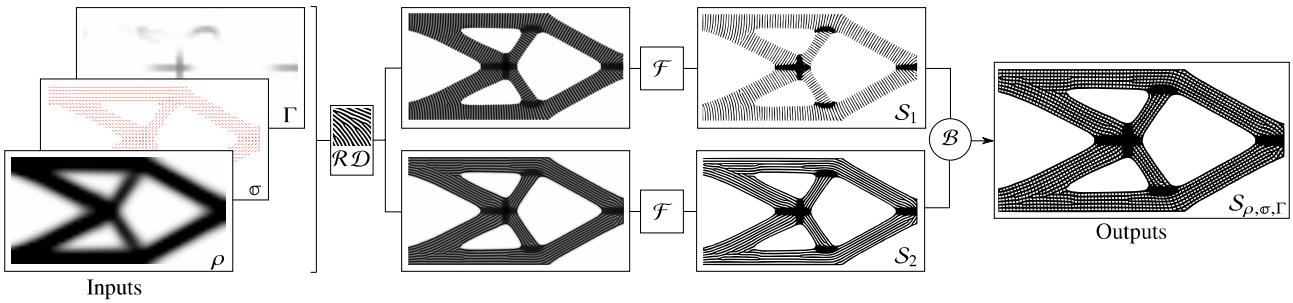

Figure 3: Global pipeline of our method. The first step ($\mathcal{RD}$) designates the Reaction/Diffusion, the intermediate step ($\mathcal{F}$) represents a filtering process while the final step ($\mathcal{B}$) is constituted of boolean operations

While these fields can be provided using arbitrary methods, we will describe them as being automatically computed from a topology optimization as it provides an interesting case of application in the context of structural optimization.

Following the latest works on the topic (Elingaard et al. (2022); Stutz et al. (2022); Groen et al. (2021); Stutz et al. (2020)), these fields can be given directly by the results from a homogenization-based topology optimization of parameterized laminates microstructures. Examples using such inputs are shown in Sec. 6.8. However we adopt here a more straightforward model for most of our examples, which can fully demonstrate the capabilities of the approach.

3.2.1 Infill Space ρ

The infill space is a density field describing the region in which the material infill should be present. We adopt a simple approach where this density field ρ is the direct output of a density-based compliance topology optimization subject to a global volume constraint. We use the material interpolation scheme known as the Solid Isotropic Material with Penalization (SIMP) approach (Bendsøe and Sigmund, 1999) in conjunction with length-scale filters (Sigmund, 1997) to obtain a well-defined boundary for the infill region. The density per element is bounded as follows:

$$0 \leq \rho(\mathbf{x}) \leq 1, \quad \forall \mathbf{x} \in \mathbf{\Omega} \tag{1}$$

A numerical optimization on a low resolution grid can be conducted following Andreassen et al. (2011). An example of results can be seen in Fig. 4b. The optimization scenario with boundary conditions and loads depicted at the top of Fig. 4a is referred to as the *cantilever* problem, a *de facto* standard test case in the literature.

3.2.2 Tensor field ϖ

The stress tensor field $\varpi(\mathbf{x} \in \mathbf{\Omega})$ can then be extracted from this preliminary optimization. For each element the tensor is diagonalizable in an orthogonal basis with real eigenvalues:

$$\varpi = \mathbb{R}\mathbb{\Lambda}\mathbb{R}^T \text{ with } \begin{cases} \mathbb{\Lambda} = \text{diag}(\sigma_i)_{i\in[\![1,d]\!]}, & |\sigma_i| \geq |\sigma_{i+1}| \\ \mathbb{R} = (\mathbf{v}_i)_{i\in[\![1,d]\!]}, & \|\mathbf{v}_i\| = 1 \end{cases} \tag{2}$$

with σ_i the principal stresses, $\mathbf{v}_i$ their associated directions (i.e. the eigenvectors) and $d \in \{2, 3\}$ the dimension considered (2 or 3).

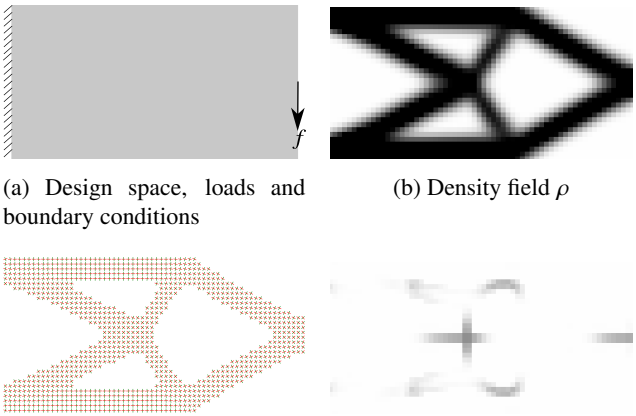

(a) Design space, loads and boundary conditions

(b) Density field ρ

(c) Stress rotation field $\mathbb{R}$

(d) Infill Map Γ_ϖ

Figure 4: Results for the Cantilever 2D on a 64×32 grid

The eigenvalues are called the principal stresses and their associated eigenvectors form a rotation matrix which characterizes the principal stress directions perpendicular to the planes where the principal stresses act. Such rotation field $\mathbb{R}(\mathbf{x})$ is shown Fig. 4c for the Cantilever2D.

As we aim to construct a lattice built upon this stress tensor field, we seek for a certain regularity in the rotation field $\mathbb{R}(\mathbf{x})$. This is not always the case where the orientation is not clearly defined ($\sigma_i \approx 0$ or $\sigma_i \approx \sigma_j$). Some regularization steps can be necessary before using this tensor field as input of our method. These steps are explained in the Appendix.

3.2.3 Infill Map Γ

The Infill Map indicates the areas to infill with homogeneous material. It can be divided into two sub-maps: the first one $\Gamma_c(\mathbf{x})$ is given by the designer constraints and the other one $\Gamma_\varpi(\mathbf{x})$ is derived from the previous rotation field.

This second map addresses an issue encountered when the input stress field is locally isotropic, or is associated to very low values. In this case, the ordering and direction of the eigenvalues become meaningless, and the extracted rotation field would exhibit discontinuities. As there is no clear orientation to follow in these regions, we propose to infill them with solid isotropic material.

To detect these regions, we propose an automatic computation assessing the local consistence of the alignment of all eigenvectors using the value

$$a(\mathbf{x}) = \frac{1}{N_\mathbf{x} d} \sum_{\mathbf{y}\in N(\mathbf{x})} \sum_{1\leq i\leq d} |\mathbf{v}_i(\mathbf{y}) \cdot \mathbf{v}_i(\mathbf{x})| \tag{3}$$

with $N(\mathbf{x})$ and $N_{\mathbf{x}}$ respectively the set and count of neighbours of the element situated in $\mathbf{x}$. We can then define $\Gamma_\varpi(\mathbf{x})$ as:

$$\Gamma_\varpi(\mathbf{x}) = (1 - a(\mathbf{x}))\rho(\mathbf{x}) \tag{4}$$

Such map for the cantilever 2D problem can be seen on Fig. 4d. The global map can then be written:

$$\Gamma(\mathbf{x}) = (\Gamma_c \cup \Gamma_\varpi)(\mathbf{x}) = \max(\Gamma_c(\mathbf{x}), \Gamma_\varpi(\mathbf{x})) \tag{5}$$

4 Pattern Growth

The concept of Turing patterns was first introduced by Alan Turing (1952) in a foundational paper. In this paper, he describes how natural patterns such as stripes, spots, spirals, fronts, targets, hexagons may arise naturally out of a homogeneous and uniform state. The original theory explains pattern formation through a Reaction/Diffusion mechanism and as of this day it remains a major theory in theoretical biology used to model embryonic development as well as skin pigmentation.

4.1 The Gray-Scott Model

In this paper we are mainly focused on a model which was first introduced by Gray and Scott (1984) to describe the kinetics of a chemical reaction. The model proposes to characterize the evolution of the concentrations $u(\mathbf{x}, t)$ and $v(\mathbf{x}, t)$ of two reactive chemical species U and V (directly linked to the visual patterns that can appear) by the following set of equations:

$$\begin{cases} \frac{\partial u}{\partial t} = \nabla \cdot (\varpi_u \nabla u) + \gamma f(u, v) \\ \\ \frac{\partial v}{\partial t} = d\nabla \cdot (\varpi_v \nabla v) + \gamma g(u, v) \end{cases} \tag{6}$$

where ϖ_u and ϖ_v represent the diffusion tensors of the two species, $d = \frac{D_v}{D_u}$ the diffusion ratio between the two species, and γ a parameter which controls the characteristic length of the pattern.

In the original model the chemical U is added in the environment at a feed rate F while the chemical V is removed at a kill rate k. Both chemicals diffuse but U diffuses faster than V ($d < 1$) to observe patterns. The reaction kinetics is hence controlled by the following functions:

$$\begin{cases} f(u, v) = -uv^2 + F(1 - u) \\ \\ g(u, v) = uv^2 - (k + F)v \end{cases} \tag{7}$$

Here we are only interested in this model as a *tool* to generate smooth oriented patterns through the integration of the PDE. The isotropic form of this equation, for $\varpi_u = \varpi_v = 1$, is a case study for pattern formation through Reaction/Diffusion in the literature. An example of typical 2D Gray-Scott pattern is shown Fig. 5.

Starting from this isotropic form, one need to control these patterns for the purpose of designing anisotropic microstructures. First, the pattern growth should be restricted inside a domain defined by a thresholding of the input Density Field ρ (section 4.2). As a second constraint, pattern should be able to grow in accordance with the input Tensor Field ϖ (section 4.3). Then the parameters F and k should be chosen wisely to generate connected structures as well as letting specific areas homogeneous according to the input Infill Map Γ (section 4.4).

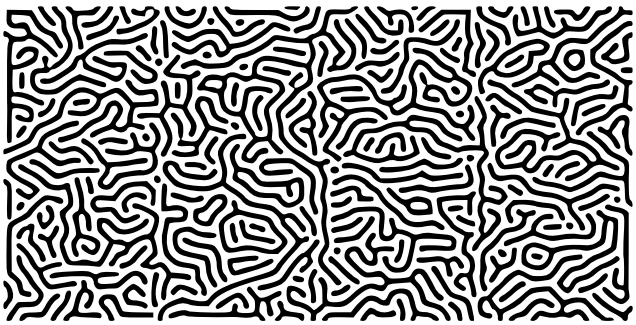

Figure 5: A typical Gray-Scott isotropic pattern called "worms" patterns: iso at 0.5 of the normalized concentration of V.

In the following, the species $(1 - U)$ is considered as the species of interest which means the density field generated by $(1 - u(\mathbf{x}))$ normalized between 0 and 1 is supposed to shape the oriented structure.

4.2 Restriction to a design area

Pattern growth can be restricted to a design region $\mathbf{\Omega} = \{\mathbf{x}, \quad \rho(\mathbf{x}) \geqslant s\}$ (for s chosen in $]0, 1[$). There are different options to enforce this constraint. Because $(1 - U)$ is considered as the species of interest, an absorbing condition for the species V is sufficient to restraint the growth, and we propose the following formulation:

$$\begin{cases} \frac{\partial u}{\partial t} = \nabla \cdot (\varpi_u \nabla u) + \gamma f(u, v) \\ \\ \frac{\partial v}{\partial t} = d\nabla \cdot (\varpi_v \nabla v) + \gamma g(u, v)\mathbb{1}_{\mathbf{\Omega}} - \lambda(1 - \mathbb{1}_{\mathbf{\Omega}})v \end{cases} \tag{8}$$

where $\mathbb{1}_{\mathbf{\Omega}}(\mathbf{x})$ takes the value 1 if $\mathbf{x} \in \mathbf{\Omega}$ and 0 otherwise. We set $\lambda > 0$ and $\lambda \gg F, k$ such that the species V as well as the species $(1 - U)$ are exponentially "killed" outside the area of interest. This is the case Fig.6 for the cantilever in the isotropic case.

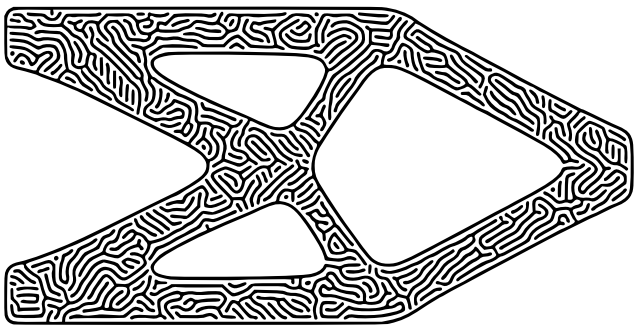

Figure 6: Gray-Scott pattern restricted inside the region where $\rho(\mathbf{x}) \geqslant 0.5$

4.3 Anisotropic Growth

Anisotropic Reaction/Diffusion can be tricky to handle when using standard finite difference approaches on a grid. We

start by explaining why and which choices and simplifications have been made to overcome these difficulties.

4.3.1 Anisotropic Reaction/Diffusion

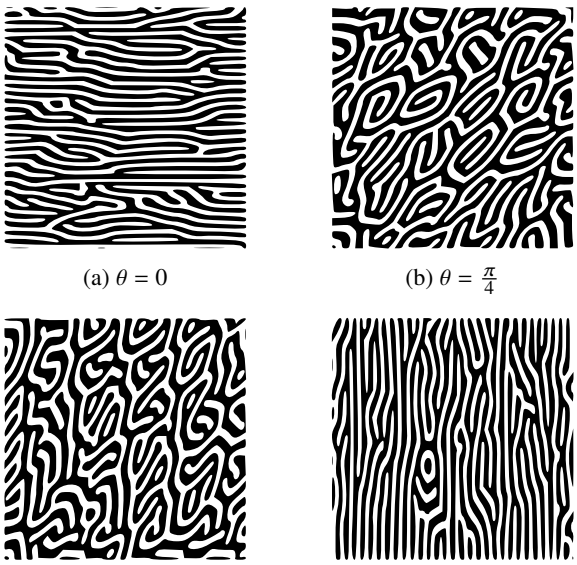

(a) $\theta = 0$ (b) $\theta = \frac{\pi}{4}$

(c) $\theta = \frac{\pi}{3}$ (d) $\theta = \frac{\pi}{2}$

Figure 7: Patterns generated when the two species are equivalently anisotropic

Anisotropic diffusion is numerically inaccurate when integrated with the finite differences on a regular grid for anisotropy directions not aligned with the axis of the grid (Umansky et al. (2005); Pérez-Grande et al. (2016); Meier et al. (2010)). It's very noticeable for extremely anisotropic cases such as in plasmas (Batischev et al. (1999); Günter et al. (2005)) and lots of methods have been proposed to address this issue in these specific cases (Soler et al. (2020); van Es et al. (2016); Tang and Wang (2017); Yang and Wang (2019)). Although it is rarely mentioned, such inaccuracy also impacts anisotropic Reaction/Diffusion systems, and the non-linear term describing the chemical reaction even amplifies this effect. Let us consider the example of a Gray Scott model with two anisotropic species with $\mathfrak{o}_u = \mathfrak{o}_v = \mathfrak{o}$ such that the first eigenvalue of $\mathfrak{o}$ is 5 times bigger than the second one, and parameters (F, k) chosen for producing worms patterns (note that there's no reason to observe Turing patterns in the general case where $\mathfrak{o}_u \neq \mathfrak{o}_v$). Fig. 7 shows some results obtained when the main anisotropic direction is rotated along an angle θ. While Fig 7a and 7d exhibits highly oriented structure when the anisotropic direction is aligned with the x or y axis of the grid, it is not the case anymore when this direction follows an arbitrary angle (Fig. 7b and 7c). In the later, a worm-like pattern is still generated, but the alignment of the synthesized patterns along the prescribed direction is clearly reduced compared to the grid-aligned direction.

Only few works have proposed the use of anisotropic Gray-Scott Reaction/Diffusion. Some were related to vector field visualization (Sanderson et al. (2004)) or texture synthesis (Witkin and Kass (1991); Kindlmann et al. (2000); Sanderson et al. (2006)) but fall out our scope as they only considered very small anisotropy magnitude. Others tackled specific anisotropy through a polar diffusive function which favour the diffusion front toward a specific directions in 2D (Kim and Lin (2007); Chi et al. (2016)), while not considering a diffusive tensor in its general form.

Interestingly, and as noted in the 2D case by Malheiros and Walter (2017), considering solely the species U to be anisotropic while letting V isotropic ($\mathfrak{o}_v$ = identity) allows to generate oriented patterns that are artifact free even when basic explicit standard first-order discretization is used for the numerical integration of the PDE. As illustrated in Fig. 9, even for a small anisotropy (here the first eigenvalue is only $\xi = 1.2$ time bigger than the second one), the synthesized patterns remain coherently oriented and their shape are independent of the orientation of the anisotropy with respect to the grid. While the method doesn't guarantee numerical accuracy, the orientation-independence of the pattern is sufficient for our purpose and the approach has the advantage to generalize trivially to 3D Reaction/Diffusion. We further show in Fig.8b and 8f an example with spatially varying orientation of the diffusion field ($\mathfrak{o}_u$). In this case, an initial diffusion field is defined on a 11×11 grid with an anisotropy $\xi = 5$ times superior on the main direction (red) than in the secondary orthogonal direction (green). The field is then interpolated on a refined grid in order to solve the Reaction/Diffusion and generate the patterns with sufficient resolution. Note that the resulting patterns are always oriented perpendicularly to the main direction of diffusion because U diffuses faster than V so the orientation is imposed by the slowest direction of diffusion of U.

To simplify the computation and avoid the evaluation of the derivative of $\mathfrak{o}$, we suppose that the field $\mathfrak{o}$ vary sufficiently slowly in space such that we can approximate $\nabla \cdot (\mathfrak{o}(\mathbf{x})\nabla) \simeq (\mathfrak{o}(\mathbf{x})\nabla) \cdot \nabla$, therefore neglecting the term $\nabla\mathfrak{o}(\mathbf{x})\nabla$. As illustrated in Fig. 8c and 8g, we check on these typical examples that the synthesized patterns obtained using the approximation remain similar to the full computation. We further compute the local average orientations of the pattern using a local 2D Fourier transform. To this end, we split the synthesized image into sub-images of 11×11 pixels that we normalize individually to a zero mean value. We then compute a FFT on each sub-image and locate its maximal modulus. The corresponding mean direction is orthogonal to the maximal frequency can therefore be visually interpreted as the direction that links the center of the patch to the maximal modulus in this 2D Fourier space. The results are presented on Fig.8d and 8h and show the correspondence with the expected directions.

The equation we use in the following to generate the anisotropic patterns is therefore the following modified version of Eq. (6)

$$\begin{cases} \frac{\partial u}{\partial t} = (\mathfrak{o}(\mathbf{x})\nabla) \cdot \nabla u + \gamma f(u, v) \\ \\ \frac{\partial v}{\partial t} = d\nabla^2 v + \gamma g(u, v) \end{cases} \tag{9}$$

4.4 Parameters selection

Optimal parameters range

In the isotropic Gray-Scott model, an exhaustive study has been conducted by Pearson (1993) to identify for which set

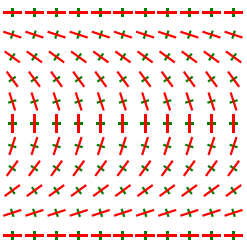

(a) $\varpi_A(\mathbf{x})$ with θ varying between 0 and π along y

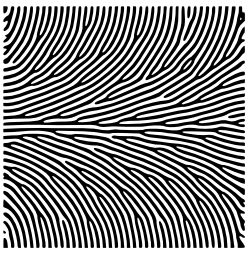

(b) Patterns generated by $\varpi_A(\mathbf{x})$ with the term $\nabla\varpi(\mathbf{x})\nabla$

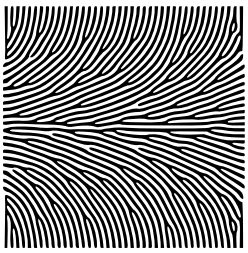

(c) Patterns generated by $\varpi_A(\mathbf{x})$ without the term $\nabla\varpi(\mathbf{x})\nabla$

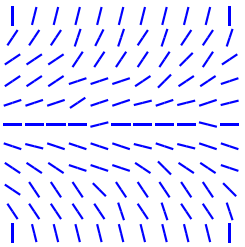

(d) Mean orientation computed from the FFT by patches

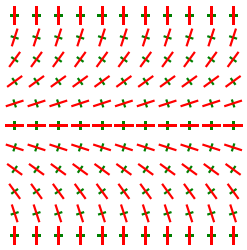

(e) $\varpi_B(\mathbf{x})$ with θ varying between $-\frac{\pi}{2}$ and $\frac{\pi}{2}$ along y

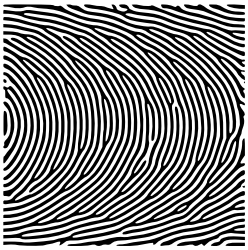

(f) Patterns generated by $\varpi_B(\mathbf{x})$ with the term $\nabla\varpi(\mathbf{x})\nabla$

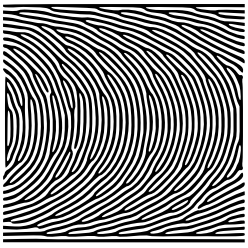

(g) Patterns generated by $\varpi_B(\mathbf{x})$ without the term $\nabla\varpi(\mathbf{x})\nabla$

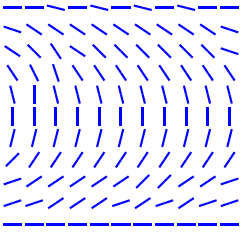

(h) Mean orientation computed from the FFT by patches

Figure 8: Oriented patterns generated by the species V on a 2D grid

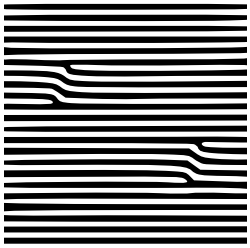

(a) $\theta = 0$

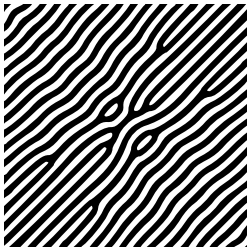

(b) $\theta = \frac{\pi}{4}$

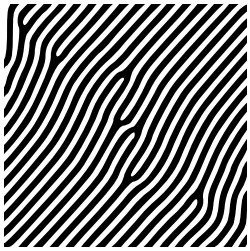

(c) $\theta = \frac{\pi}{3}$

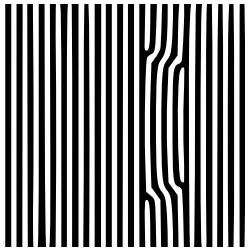

(d) $\theta = \frac{\pi}{2}$

Figure 9: Patterns generated when only one species is anisotropic

of (F, k) patterns can be observed and of which type. To this end, the Reaction/Diffusion is simulated for different values of F and k to construct a map (F, k) depicting the different areas where patterns can emerge.

In our case, we aim at finding the optimal parameters (F, k) in the anisotropic case such that the synthesized patterns are both well aligned with the prescribed direction and fairly connected so that it creates continuous paths without end points. We thus propose to conduct the same study with a discretization of the space (F, k) into duplicated patches where the anisotropy is locally controlled by the tensor ϖ_B introduced Fig. 8e. The map is simulated on a 4000×4000 grid, subdivided in patches of size 100×100 where the Reaction/Diffusion is oriented by ϖ_B inside each patch, and for F, k varying from 0 to 0.1 along the whole grid.

Such map is shown in Fig. 10, and it allows to observe which kind of pattern are synthesized in the anisotropic case depending on the values of F and k. Similarly to the isotropic case, patterns tend to appear on a curved front, thus F and k need to be chosen in this area of interest. In addition, the connectivity of the pattern is not the same everywhere. For a fixed value of F, one can notice for instance that patterns are getting less connected from left to right. As we are interested in connected patterns as they preserve longer paths, we will choose some sets of (F, k) which favour this behaviour. The area bounded in red Fig. 10 delimits the values (F, k) which correspond to this desired behaviour. Choosing a set of (F, k) outside this area will either show no pattern at all (plain or empty fill in the most-left/right side) or patterns with disconnected components (right-neighborhood of the circled area). We chose experimentally $F = 0.0395$ and $k = 0.0595$ in all our simulations. These values correspond to a mid-point of the circled region, but we note that selecting other values in the admissible region are associated with similar results.

Infill a specific area

As explained in Sec. 3.2.3, the scalar field $\Gamma(\mathbf{x})$ is used to indicate where the model should be filled with plain material. To represent this effect within the Reaction/Diffusion process, we extend the value k to a space-varying field defined as

$$k(\mathbf{x}) = k\,(1 - \alpha\Gamma(\mathbf{x}))\,. \tag{10}$$

This allows to "kill" V (and so $(1 - U)$) conformly to the Infill Map, while the parameter $\alpha \in [0, 1]$ is used to adjust how much these regions should be infilled.

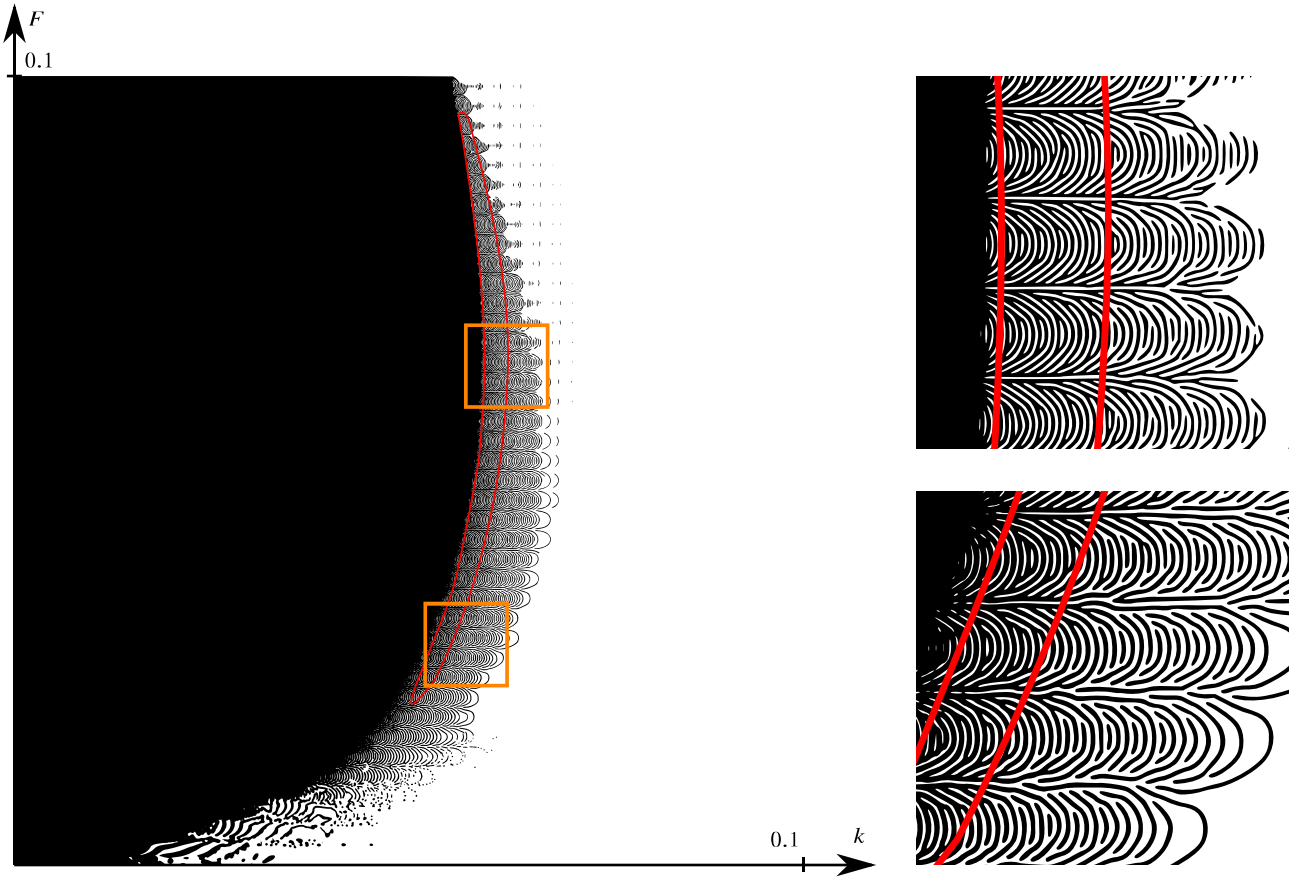

Figure 10: The (F, k) map for the anisotropic Gray-Scott model (iso at 0.5). The bounded area in red shows the acceptable values for F and k in the simulation. The zooms show clearly the variations of pattern connectivity

4.5 Reaction/Diffusion along multiple directions for lattice generation

Our objective is to generate a lattice structure from the synthesized patterns. To this end, we consider d independent Reaction/Diffusion processes, with $d = \{2, 3\}$ being the dimension of the embedding. Each process $i \in [0, d-1]$ uses its own diffusion tensor $\mathfrak{o}_i$ with a main direction of anisotropy oriented orthogonally to the expected growing pattern (a curve in 2D, and a surface in 3D), and two different processes are set to have orthogonal main anisotropic directions. We detail in the following the complete formulation used for these processes

Tensor guided patterns

Our input tensor can be written $\mathfrak{o} = \mathbb{R}\mathbb{\Lambda}\mathbb{R}^T$, potentially after some regularization of $\mathbb{R}$ as explained in 3.2.2. If we define $\xi > 1$ our custom anisotropy we can define one diffusion tensor for each principal direction i as:

$$\mathfrak{o}_i = \frac{1}{\mathrm{Tr}(\mathbb{D}_i)} \mathbb{R}\mathbb{D}_i\mathbb{R}^T \tag{11}$$

where $\mathbb{D}_i$ is a diagonal matrix filled with 1 on the diagonal and ξ at the (i, i) position. This will generate patterns oriented along each principal direction of the input tensor field.

Stress oriented structures

Compared to classical structural optimization schemes, no finite element analysis of the structure is being performed. Our method can be seen as a "post processing" from the result of the optimization via the Reaction/Diffusion equations.

Gathering all together we can now generate structures infilled with patterns perpendicular to each principal directions of the input tensor field. Each structures $\mathcal{S}_i$ is represented by a normalized density field obtained by the finite differences integration of each following system:

$$(\mathcal{S}_i) \begin{cases} \frac{\partial u_i}{\partial t} = (\mathfrak{o}_i(\mathbf{x})\nabla) \cdot \nabla u_i + \gamma f(u_i, v_i) \\ \frac{\partial v_i}{\partial t} = d\nabla^2 v_i + \gamma g(u_i, v_i)\mathbb{1}_{\mathbf{\Omega}} - \lambda(1 - \mathbb{1}_{\mathbf{\Omega}})v_i \\ f(u_i, v_i) = -u_i v_i^2 + F(1 - u_i) \\ g(u_i, v_i) = u_i v_i^2 - [k\,(1 - \alpha\Gamma(\mathbf{x})) + F]\, v_i \\ u_i(\mathbf{x}, t = 0) = 1, \quad \begin{cases} v_i(\mathbf{x} \in \mathcal{D}_0, t = 0) = 1 \\ v_i(\mathbf{x} \notin \mathcal{D}_0, t = 0) = 0 \end{cases} \end{cases} \tag{12}$$

where $\mathcal{D}_0$ designates the initial "seed", typically a small disk (in 2D) or sphere (in 3D) with at least a portion included in the *infill space*. This small initial seed was preferred to a large initial and possibly random covering of the infill space, as we noticed experimentally that the Reaction/Diffusion

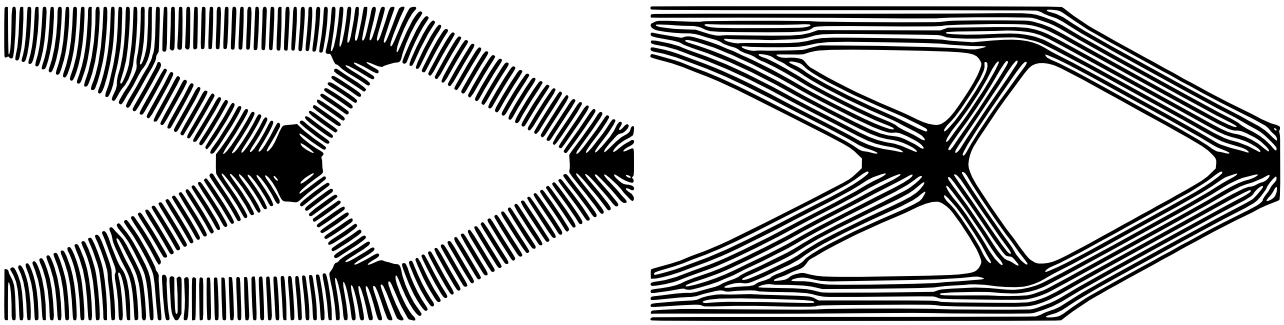

(a) $(\mathcal{S}_1)$ (b) $(\mathcal{S}_2)$

Figure 11: Stress oriented structures for the cantilever 2D generated on 1280×640 mesh, iso at 0.7

process generates more conforming patterns when these are developed as growth through empty space. Nonetheless it is possible to speed up the structure generation by choosing an initial state made of several seeds $\mathcal{D} = \cup_i \mathcal{D}_i$ as long as they are sufficiently spaced. Fig.11 show the resulting structures generated by an isosurface extraction of the density fields $s_i = 1 - u_i$ for the cantilever. Note that for a given resolution the parameter γ controls the number of lines contained in a slice of material (i.e. the wavelength) whereas the chosen isosurface controls their size.

4.6 Numerical Implementation

To solve Eq. 12, we use a straightforward finite explicit difference scheme. First the values are discretized on a regular squared grid to compute the terms $(\sigma(\mathbf{x})\nabla)\cdot\nabla u$ and $\nabla^2 v$ by second order finite differences. This reduces the computation to an Ordinary Differential Equation (ODE). This ODE can then be discretized in time t and solved by a first order explicit scheme:

$$\begin{cases} u^{t+1} = u^t + \left(\frac{1}{\Delta x^2}\mathcal{L}^{\sigma} * u^t + \gamma f(u^t, v^t)\right)\Delta t \\ v^{t+1} = v^t + \left(\frac{d}{\Delta x^2}\mathcal{L} * v^t + \gamma g(u^t, v^t)\mathbb{1}_{\mathbf{\Omega}} - \lambda(1-\mathbb{1}_{\mathbf{\Omega}})v^t\right)\Delta t \end{cases} \tag{13}$$

Here $\mathcal{L}^{\sigma}*$ and $\mathcal{L}*$ represent the discrete spatial operators which can be written in the form of convolutions. Δx and Δt are the disretization steps in space and time. While solving the isotropic heat equation using such explicit scheme would require the condition $\Delta t/\Delta x^2 < \frac{1}{2}$ to converge, we found in practice that we had to slightly lower this bound in the Reaction/Diffusion case, and $\Delta t/\Delta x^2 < 1/8$ was found to be sufficient in the examples shown in our results.

Reaction/Diffusion is a constantly evolving process that may never reach a real static fix-point state. Even when the main structures have grown and reached the boundaries, local oscillations and species concentration swaps between u and v can occur in the branching regions of the patterns. We, therefore, cannot check for local convergence criteria for each pixel/voxel of the discrete structure. Instead, we propose an automatic stopping criteria that only considers the design changes at a more global scale. To this end, we interpret the value u at a given pixel/voxel as being a weighted area/volume. Our general idea is to stop the time integration when the change of volume of the structure becomes sufficiently small.

$$\mathcal{G}^t = \frac{1}{V_{\mathbf{\Omega}}}\left|\frac{\partial V_S}{\partial t}\right| = \frac{1}{V_{\mathbf{\Omega}}\Delta t}\left|\sum_{\mathbf{\Omega}}(u^{t+1} - u^t)\right| < \varepsilon, \tag{14}$$

where $V_{\mathbf{\Omega}}$ is the volume (resp. the area in 2D) of the design region, and $\frac{\partial V_S}{\partial t}$ is its change along the current time step. $\mathcal{G}^t$ measures the relative volume (resp. area) of the structures that are still in the growth phase, and its value will decrease after having passed through one or several maxima, as shown in Fig. 12 for the cantilever. We used $\varepsilon = 10^{-7}$ in all our examples. From this figure, one can also notice that the growth is slower (about 2 times for the cantilever initialized with one seed in the center) for the pattern oriented perpendicularly to the first direction $(\mathcal{S}_1)$ than for the one lined up. More precisely, the high frequency oscillations on $\mathcal{G}_1^t$ correspond to the emergence the parallel stripes which grow perpendicularly to the first stress direction. The same scenario goes for the three oriented structures generated for the chair Fig. 24 and whose the $\mathcal{G}^t$ can be visualised Fig. 13. The condition $\mathcal{G}^t < \varepsilon$ therefore allows to continue the evolution as long as new branching elements are generated as this is associated to a change of the volume, while being able to stop when only local oscillations take place as this global volume does not change anymore.

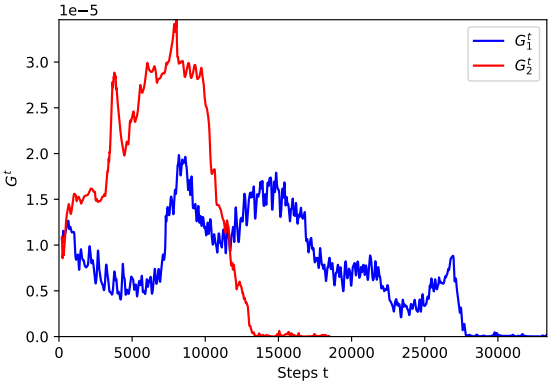

Figure 12: $\mathcal{G}^t$ for the two stress oriented structures of the cantilever

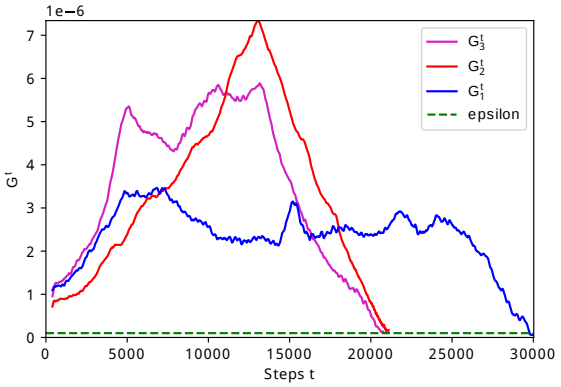

Figure 13: $\mathcal{G}^t$ for the three stress oriented structures of the chair

5 Structure Compilation

Eventually by merging the different substructures infilled with oriented patterns along the principal stress directions, it is possible to generate a shape with oriented lattice. However, while the generated microstructures are oriented in conformity with the local stress directions, they are not associated with an optimized response to the stress magnitude. To get closer to optimized structures, we add a pattern rescaling filter to adapt the structure patterns thickness on a qualitative basis (section 5.1) before combining them (section 5.2).

5.1 Pattern rescaling filter

Qualitative rescaling

Bendsøe and Kikuchi (1988) introduced the unit-cell with a rectangular hole as it constitutes an optimized microstructure compared to a regular square cell (Fig. 14).

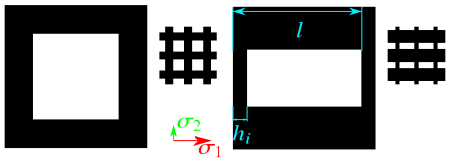

Figure 14: Layout of the unit-cell with a square hole (left) and with a rectangular hole (right) optimized for the stress tensor (σ_1, σ_2)

Following this idea, in order to enhance the structural performance relatively to the mass, one can shift qualitatively the iso according to whether the substructure is oriented along the first principal direction or not to enlarge the pattern oriented along the first principal stress directions while reducing the width of the others. Assuming that s_i has been rescaled between 0 and 1, this can be achieved by redefining the density fields as follow

$$\tilde{s}_i = \max\left(\min(s_i, 1 - \mu_i + \delta_i), 1 - \mu_i - \delta_i\right) \tag{15}$$

where μ_i denotes the relative thickness according to the direction i and δ_i a parameter which applies a threshold favouring a binary structure while preserving its smoothness.

Minimum member size

Because our structure aims to be manufactured, we need to guarantee that the minimum strut diameter or wall size of the lattice can be fabricated. This means that we need to make sure that the smallest features from $\tilde{s}_i$ are resolved by a minimum number of pixels h_{min}. The parameter l in Fig. 14 denotes the wave-length (in pixel/period) of the pattern periodicity, which is the same for the different directions because of the way the diffusion tensors were built. The relative thickness μ_i is linked to the width of the pattern h_i (in pixel) by:

$$\mu_i = \frac{h_i}{l} \tag{16}$$

As the smallest features have to be resolved by at least h_{min} pixels, it constrains μ_i to be greater than $\mu_{min} = \frac{h_{min}}{l}$. For instance, in the cantilever structures generated Fig. 11 on a 1280×640 mesh, if we want the smallest features resolved by at least 1 pixel, we measured a wavelength of pattern periodicity of $l \simeq 15$ pixels/period pixel and so $\mu_i \geq 0.07$.

A bilinear upsampling from the actual mesh to a finer mesh may be performed if one wants to use a smaller value for μ_{min}.

Variable thickness

In its simplest form, the proposed filter re-scales the density fields for each of the principal directions and yields a uniform porosity of the infill (except, of course, in the fully-solid region Γ). The resulting pattern has a consistent length-scale but this also leads to a sub-optimal design compared to methods allowing a graded porosity. As demonstrated in the section 6, our filter can be replaced by the last step of the post-processing procedure from Elingaard et al. (2022) to allow spatially varying thickness of the pattern. As a matter of fact, $D_i(\mathbf{x}) = 1 - s_i(\mathbf{x})$ can be seen as a distance field and the thickness of its implicit skeleton can be controlled using a lamination width $\mu_i(\mathbf{x})$ to adaptively threshold the density field where $\mathbb{H}(\mathbf{x})$ is the Heaviside step function:

$$\tilde{s}_i(\mathbf{x}) = \mathbb{H}(\mu_i(\mathbf{x}) - (1 - s_i(\mathbf{x})) \tag{17}$$

5.2 Boolean Operation

The final structure can be generated through the use of binary merging operators of implicit surfaces, corresponding to the use of min and max functions on their field values

$$(\mathcal{S}) \begin{cases} \mathcal{S}_{2D} = \mathcal{S}_1 \cup \mathcal{S}_2 = \max(\tilde{s}_1, \tilde{s}_2) \\ \mathcal{S}_{3D} = \bigcup\limits_{i \neq j} \mathcal{S}_i \cap \mathcal{S}_j = \max\limits_{i \neq j} \left(\min\limits_{i \neq j} (\tilde{s}_i, \tilde{s}_j) \right) \end{cases} \tag{18}$$

The results for the cantilever is shown Fig. 15 and different examples in 2D and 3D with structural analysis validation are given in the next section.

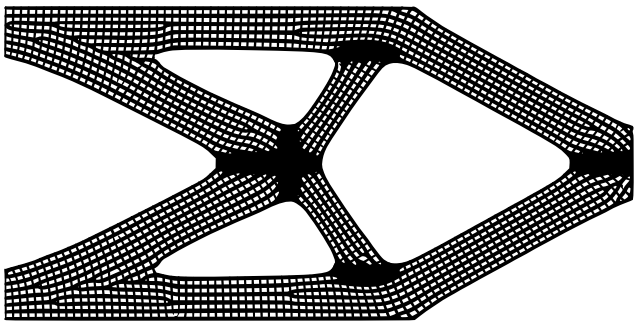

Figure 15: Final structure for the cantilever 2D, with $\mu_1 = 0.3$ and $\mu_2 = 0.12$

6 Results and analysis

This section provides various numerical examples, in 2D and 3D, which demonstrate the capability of our method. The common parameters used in all of our examples are summarized Table 1, while Table 2 presents the relative thickness values μ_i.

Param.	d	γ	F	k	α	ξ	δ_i
Value	0.5	1	0.0395	0.0595	0.5	5	0.01

Table 1: Parameters and associated values in every example

Model	μ_1	μ_2	μ_3
Cantilever 2D Fig. 15	0.12	0.3	.
L-Beam Comp. 2D Fig. 18	0.15	0.4	.
L-Beam Stress 2D Fig. 18	0.15	0.4	.
Bridge MoLC 2D Fig. 19a	0.15	0.4	.
Bridge MuLC 2D Fig. 19b	0.15	0.4	.
Bracket MoLC 3D Fig. 1	0.15	0.25	0.25
Bracket MuLC 3D Fig. 21	0.15	0.25	0.25
MBB Beam 3D Fig. 22h	0.20	0.25	0.25
Chair 3D Fig. 24b	0.20	0.25	0.25

Table 2: relative thickness values μ_i

The structures shown on our result figures are generated from iso curves (in 2D) or iso surfaces (in 3D) extraction from the pixel/voxel representation. The experiments were run on a PC workstation with an Intel Xeon Gold 6148 CPU running at 2.40GHz, 128 GB RAM and a Nvidia Quadro RTX 6000 with 24 GB memory. Our implementation is based on PyTorch library in Python to store the 2D and 3D grids as *PyTorch-tensors*. The spatial finite difference operators are computed as convolutions and benefit from the parallel execution on the GPU. For memory and speed reasons we employed Half-precision float numbers for all the computations.

6.1 Computational times

We present in Table 3 the timings of the method for the different examples. This table presents respectively: The input resolution on which the stress tensor or an optimized material orientation has been computed; The resolution of the upsampled grid on which the Reaction/Diffusion PDE is numerically solved, and its corresponding number of pixels/voxels #Ele.; The spatial interval Δx and time step Δt considered; The total time $T_{RD}^{\mathcal{S}_1}$ for the structure $\mathcal{S}_1$ to grow from the initial condition shown Fig. 16 with the number of iterations #It. to achieve it.

In standard conditions, we started the complete growth of the Reaction/Diffusion process in setting a small disk/sphere of uniform density $u = 1$ placed inside the design space, with a radius of $0.05 \times \max_{i=x,y,z} L_i$ where $L_x \times L_y \times L_z$ is the resolution of the mesh. The total timings range from tens of seconds for the simple 2D examples to about an hour and a half for the more detailed 3D case (the chair model). Note that these timings can be reduced in seeding more initial disc/spheres within the design space (see bottom right corner of Fig. 16). This seeding strategy allows to start the growing process in multiple places, therefore saving time compared to waiting for the RD to diffuse from a single center – see Chair 3D Fig. 24b. takes 95min VS Chair 3D with mult. seeds reduced to 23 min. In this specific example the quality of the final structure is similar. However this additional seeding strategy must leave enough space between the filled disc (at least the disc diameter) for the RD to grow as expected, otherwise the oriented patterns cannot fully generate themselves leading to badly-aligned pattern as shown Fig. 17. The quality of the structure generated with this seeding strategy also strongly depends on the topology of the Infill Space, making it difficult to find a formal criteria minimizing the computation time without sacrificing pattern quality.

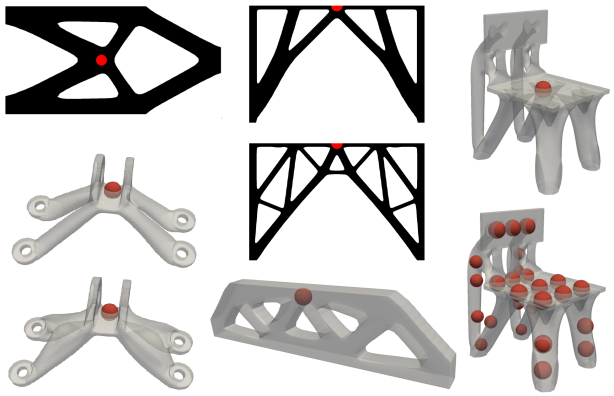

Figure 16: Initial conditions and seed regions for the models referenced in Table 3

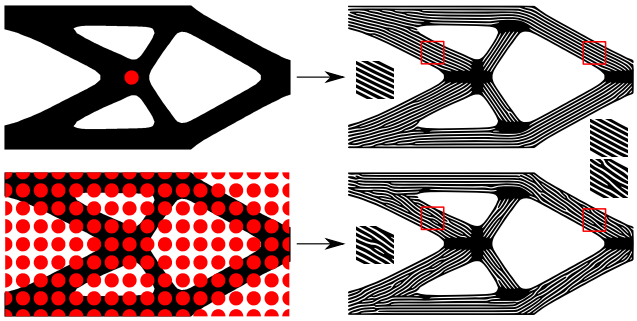

Figure 17: Effect of the initial seeding on the quality of the pattern orientation on the example of the Cantilever.

The last column of Table 3 $T_{2\%}$ provides the timing spent for the structure to locally reconstruct itself for local modification spanning an area of 2% of its infill space volume.

In this last case, we consider a fully grown structure, and locally "damage/reset" it by setting the value inside a small disk (resp. sphere) with an area set at $2\% V_\Omega$ to be 0. $T_{2\%}$ corresponds to the time needed to the Reaction/Diffusion to refill this empty space again. Note that this local adaptation is much faster than a full RD grows, and our approach is therefore able to provide an efficient solution for local shape modification.

6.2 Optimized 2D input: L-Shaped Beam

In this example, the inputs are generated from a L-Shaped Beam problem whose the loads and boundary conditions are depicted at the top of Fig. 18. We run two topology optimizations minimizing compliance or peak stress both under the same mass constraint. From the results of these optimizations, our method grew the two lattice structures displayed in the center and bottom of Fig. 18 for the compliance and peak stress minimization inputs respectively.

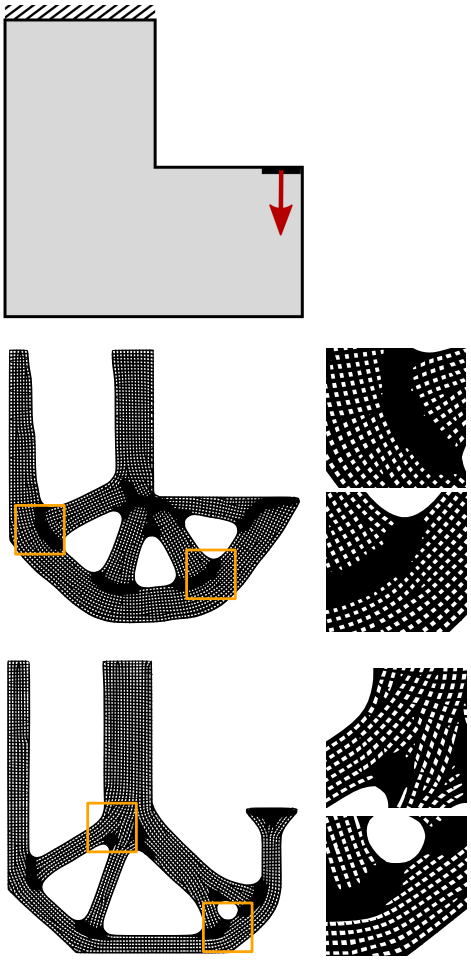

Figure 18: L-Shaped Beam generated on a 800×800 grid, from tensor fields calculated on a 80×80 grid.

We observe that the re-entrant corner is avoided in the stress minimization case. A high resolution numerical analysis of the resulting structures reveal that the stress optimized structure achieves a peak stress 63% lower than the the compliance optimized structure. This demonstrates that the proposed approach can successfully generate coherent oriented microstructures in a variety of optimization problems.

6.3 Optimized shape for multiple load cases: 5-load bridge

A common industrial requirement is the ability to optimize structures under multiple load cases. By definition, this precludes the use of the stress field to guide the design due to its non-uniqueness. In general, microstructures aligned with the stress tensor field of one load-case will yield sub-optimal anisotropic pattern orientations for all the other load cases. Since our approach is compatible with any sufficiently smooth orientation field, it therefore does not require the use of stress tensors to guide the pattern growth.

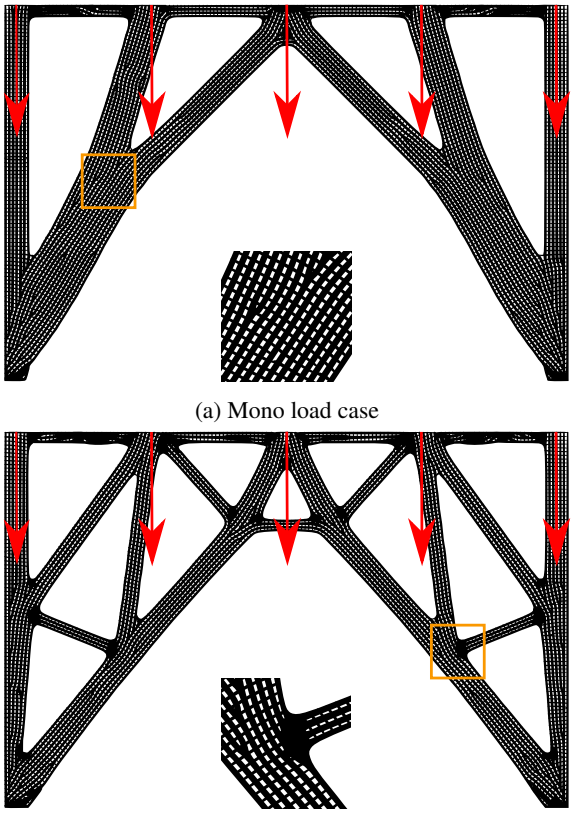

(a) Mono load case

(b) Multi load case

Figure 19: Five-load bridge: (1200×800)

The present section illustrates how the reaction diffusion process can instead be guided by a topology optimization using an orthotropic material law and considering both local material density and orientation as design variables optimized for one or multiple load cases (Schmidt et al., 2020) according to the following formulation:

$$
\begin{aligned}
\arg\min_{\boldsymbol{\rho},\boldsymbol{\alpha}} \quad & J(\boldsymbol{\rho},\boldsymbol{\alpha}) = \left(\sum_{i \in \boldsymbol{LC}} \left(\boldsymbol{f_i}^T \boldsymbol{u_i} \right)^p \right)^{1/p} \\
s.t. \quad & \boldsymbol{K}(\boldsymbol{\rho},\boldsymbol{\alpha})\boldsymbol{u_i} = \boldsymbol{f_i}, \quad \forall i \in \boldsymbol{LC} \\
& 0 \leq \rho_e \leq 1, \quad \forall e \in \boldsymbol{\Omega} \\
& -\pi \leq \alpha_e \leq \pi, \quad \forall e \in \boldsymbol{\Omega} \\
& G(\boldsymbol{\rho}) = \frac{1}{G^\star v_\Omega} \sum_{e \in \boldsymbol{\Omega}} (\rho_e v_e) - 1 \leq 0
\end{aligned}
\tag{19}
$$

Model	Input resolution	R/D Resolution	♯Ele.	Δx	Δt	$T_{RD}^{\mathcal{S}_1}$	♯It.	$T_{2\%}$
Cantilever 2D Fig. 15	64×32	1280×640	819k	1.7	1.1	30s	28k	3s
L-Beam Comp. 2D Fig. 18	80×80	800×800	640k	2.4	1.05	44s	34k	5s
L-Beam Stress 2D Fig. 18	80×80	800×800	640k	2.4	1.05	55s	42k	5s
Bridge MoLC 2D Fig. 19a	150×100	1200×800	960k	2.8	1.35	1m04s	54k	5s
Bridge MuLC 2D Fig. 19b	150×100	1200×800	960k	2.8	1.35	1m02s	52k	4s
Bracket MoLC 3D Fig. 1	$44 \times 74 \times 119$	$308 \times 518 \times 833$	133m	2.4	1.35	64m33s	19k	5m49s
Bracket MuLC 3D Fig. 21	$44 \times 74 \times 119$	$308 \times 518 \times 833$	133m	2.4	1.35	66m10s	19k	6m01s
MBB Beam 3D Fig. 22h	$4 \times 16 \times 64$	$32 \times 128 \times 512$	2.1m	2.4	1.35	34s	9k	2s
Chair 3D Fig. 24b	$140 \times 100 \times 200$	$504 \times 360 \times 720$	131m	3	1.35	95m33s	30k	4m28s
Chair 3D w/ mult. seeds	$140 \times 100 \times 200$	$504 \times 360 \times 720$	131m	3	1.35	23m17s	7k	4m28s

Table 3: Computational performance on the different scenarios presented in the article.

The orthotropic material constitutive law of each finite element e in the design space Ω is parameterized by two design variables ρ_e and α_e. We chose an orthotropic material law with the principal direction 3 times stiffer than the transverse direction. The design variables ρ describe the density distribution similarly to classical density-based topology optimization. The design variables α describe the material orientation as 1 or 3 rotation angles per element in 2D and 3D respectively. The stiffness matrix $\boldsymbol{K}$ is assembled based on the values of the design variables. Then, for each nodal force vector $\boldsymbol{f_i}$ corresponding the the load-cases $i \in \boldsymbol{LC}$, the nodal displacement vector at equilibrium $\boldsymbol{u_i}$ is computed. The objective function J is a p-Norm aggregation of compliances of each load-case with $p = 8$ thereby minimizing the highest compliance across all load cases. An inequality constraint G on the maximum allowed volume $G^\star = 0.3$ is applied based on the design space volume v_Ω and element volumes v_e. The derivatives $\frac{\delta J}{\delta \rho}$, $\frac{\delta J}{\delta \alpha}$, $\frac{\delta G}{\delta \rho}$ and $\frac{\delta G}{\delta \alpha}$ are obtained via adjoint analysis or analytical derivation and the optimization problem is solved using the MMA gradient-based optimization scheme (Svanberg, 1987).

Using a simple test scenario of a bridge with 5 loads applied at the top of the design domain we produce two sets of optimized density and orientation fields ρ and α. The first set was optimized considering all 5 loads applied simultaneously as a single load-case while the second set considered the loads applied separately as 5 distinct load-cases. We guide the anisotropic reaction diffusion process using these two sets of density and orientation field and obtain the designs in Fig. 19a and Fig. 19b for the single and multiple load-cases scenarios respectively.

We compare the performance of both designs in Fig. 19a and 19b by running a high-resolution finite element analysis for each of the 5 load-cases. The comparison is shown in Fig. 20 where one can clearly see that the pattern growth capitalizes on considering both material orthotropy and multiplicity of load-cases. The design optimized for multiple load cases achieves a significantly lower overall compliance as well as a a smaller variation in compliance across all load-cases.

6.4 Optimized 3D input: GE Bracket

Fig. 1 and Fig. 21 show a lattice structure for the *GE Bracket* (GrabCAD (2013)). The former is generated using the stress of an input which has been optimized for a single-load case

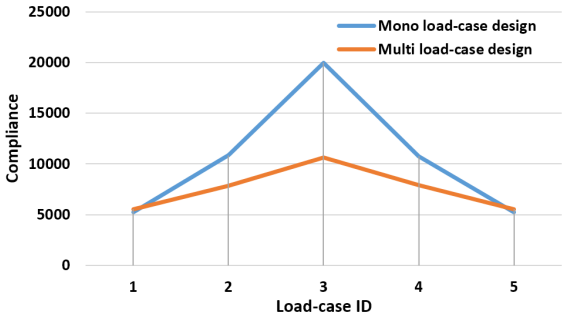

Figure 20: Comparison of the final compliances of designs in Fig. 19a and 19b for each of the 5 load cases where the load-case are numbered from left to right.

while the latter input had its material orientation optimized for a multi-load case scenario.

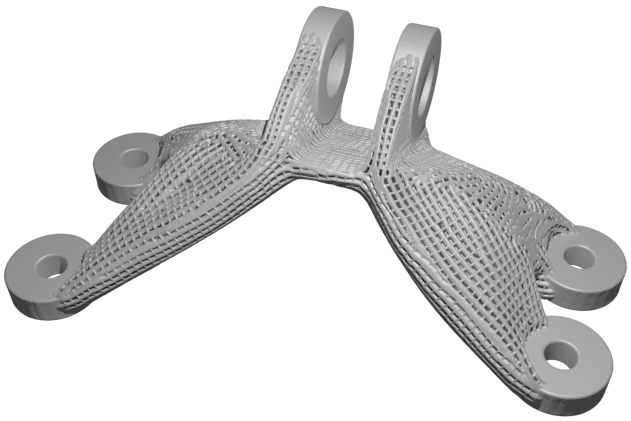

Figure 21: Our *GE Bracket* built from an input material orientation optimized for a multi-load case scenario

6.5 Optimized 3D input: MBB Beam

Fig. 22 shows the different steps for the MBB Beam case in 3D. Starting from a rectangular cuboïd Design Space (22a), the Infill Space (22b) is computed by Topology Optimization. Then the Stress Tensor (22c) can be extracted with the Infill Map (22d). From these inputs, 3 oriented structures (22e, 22f, and 22g) are generated. These structures are composed of foiled patterns in 3D. Each intersection of these oriented structures taken two at a time gives the intermediate shapes (22i), (22j) and (22i) composed of beam oriented along the principal stress directions. The union of these three

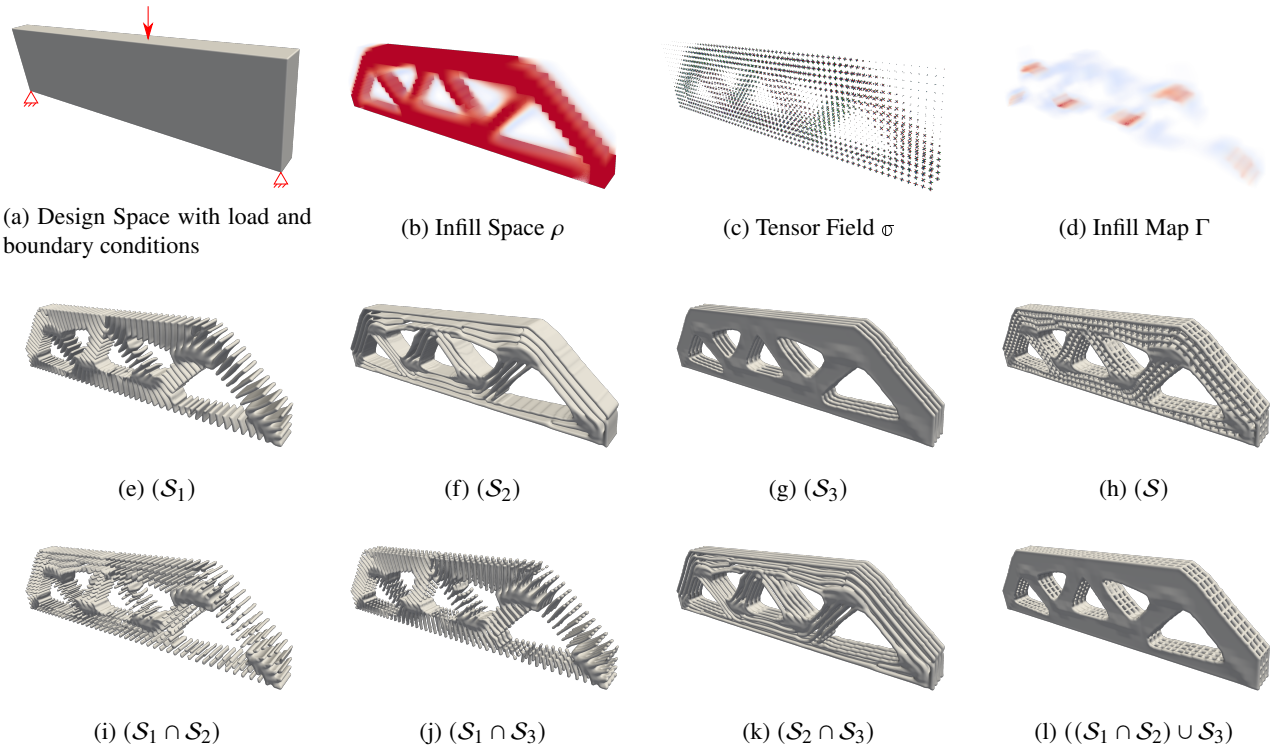

(a) Design Space with load and boundary conditions

(b) Infill Space ρ

(c) Tensor Field ϖ

(d) Infill Map Γ

(e) $(\mathcal{S}_1)$

(f) $(\mathcal{S}_2)$

(g) $(\mathcal{S}_3)$

(h) $(\mathcal{S})$

(i) $(\mathcal{S}_1 \cap \mathcal{S}_2)$

(j) $(\mathcal{S}_1 \cap \mathcal{S}_3)$

(k) $(\mathcal{S}_2 \cap \mathcal{S}_3)$

(l) $((\mathcal{S}_1 \cap \mathcal{S}_2) \cup \mathcal{S}_3)$

Figure 22: The original Design Space is $32 \times 16 \times 4$ while the final structures are generated on a $256 \times 128 \times 32$ grid

structures form the final lattice-like structure (22h). Additionally other interesting combinations can be made such as (22l) which preserves membrane-like structures along the plane stress direction and lattice in the transverse direction.

We ran a comparative Finite Element Analysis between (22h) and (22l). The shift of isosurfaces of the two structures have been made such that they present the same mass. It comes out that the membrane-like structure (22l) shows a compliance and peak von Mises stress respectively 6% and 7% lower than the lattice-like structure (22h).

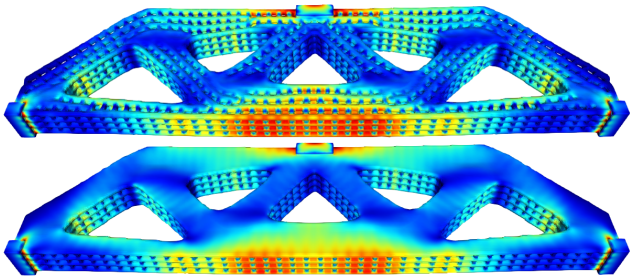

Figure 23: Visualisation of the von Mises stress for the lattice like-structure (top) and for the membrane-like structure (bottom)

6.6 Highly detailed structure: 3D Chair

Our method also demonstrates great lattice regularity. As an example of highly detailed structure, Wu et al. (2021b) proposed an optimized lattice chair (Fig. 24b) relying on a Topology Optimization with oriented homogenized material performed on a resolution of $140 \times 100 \times 200$ (using a design domain with external loads shown Fig. 24a), and followed by a parameterization optimization algorithm to design the lattice.

Using the same underlying tensor field kindly shared by them, the growth by our method on a $504 \times 360 \times 720$ grid is shown Fig. 24c. Ours does not provide an explicit truss graph but shows more lattice regularity especially near the surface of the object due to the aptitude of the Reaction/Diffusion to smoothly grow along the overall 3D shape. Although our structure looks more regular, it should be emphasized that our method only takes into account the orientation given by the tensor field. In particular, our approach does not take into account a variation of porosity in the parameters of the unit cell, therefore leading to a globally sub-optimal structure compared to the original result.

6.7 Non-linear Structural Analysis

The present section summarizes the results of a non-linear numerical analysis comparing two design variants for the MBB Beam scenario. The two design variants are obtained with a classical compliance-based topology optimization and with the proposed Reaction-Diffusion approach, respectively referred to as TO design and RD design in the following. Both models have the same total volume and are discretized with approximately 2.5×10^5 second-order quadrilateral finite elements yielding about 10^6 finite element nodes in the non-linear numerical analysis.We run a general non-linear analysis in Abaqus 2021 and retrieve the force-displacement curves shown in Fig. 25.

Several observations can be made from this non-linear analysis. The force-displacement curves of both design initially start with a roughly linear portion where the displacement is proportional to the applied force. In this linear portion, the steeper slope indicates that the TO design achieves a higher stiffness, which is to be expected because it was specifically optimized for maximum stiffness. However, at a load magnitude of approximately $140000N$ the TO design

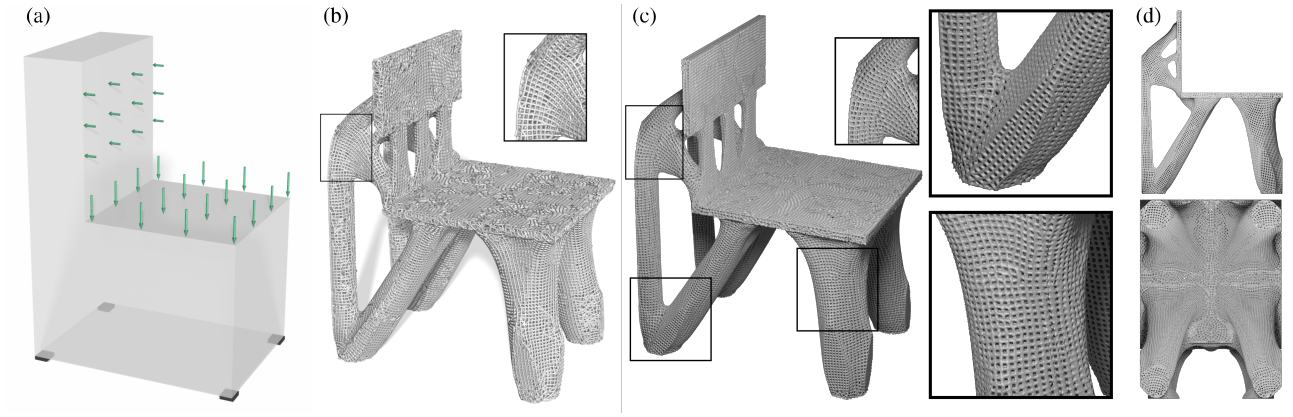

Figure 24: Optimized lattice chair: (a) Design Space with constraints (b) Optimized lattice chair generated by Wu et al. (2021b) (c) Our version on a $504 \times 360 \times 720$ mesh grid using the same underlying tensor field (d) Right and Bottom views of our optimized lattice chair. (a) and (b) reprinted with the permission of Wu et al. (2021b).

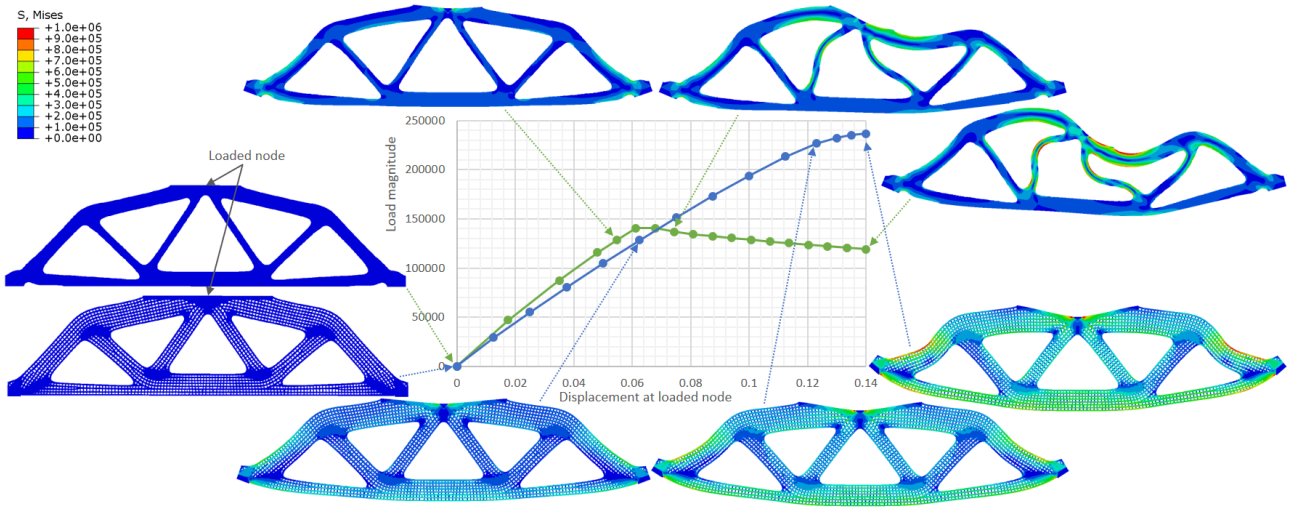

Figure 25: Force-Displacement curves for the TO design variant (in green) and the RD design (in blue) in the MBB Beam scenario. The models are displayed at different times during the non-linear analysis and color-coded by their von Mises stress.

undergoes in-plane buckling and collapses. In contrast, the RD design shows near-linear deformation up to a load magnitude of 200000N, and supports a peak load approximately 70% higher than the TO design. Finally, when approaching peak carrying load, the RD design shows a smooth and progressive failure instead of the sudden collapse of the TO design. All these findings are in good qualitative agreement with the validation by physical experiment conducted in (Wu et al. (2021b)) despite using an entirely different strategy to generate the oriented lattice-like structures. Finally, these findings are also in agreement with the general theory that lattice structure allow trading some stiffness in the expected loading conditions for a gain in stability, resistance to buckling, robustness to unexpected loading conditions, etc. Looking more closely at the RD design near peak carrying load shown in Fig. 26 allows making additional observations.

We can see that, despite being thinner, the transverse bars in the structure are generally under low stress. This confirms that their main role is to prevent bending thereby improving resistance to buckling by increasing the second moment of area of the macroscopic structural members. This also indicates that the generated microstructure is correctly oriented since the thicker primary structure carries the loading while the thinner secondary structure provides stability. We observe that the solid regions at the connection of macroscopic structural members do not show high stresses, meaning that the transition from lattice-like microstructure to solid material does not introduce stress concentrations, and this strategy might in fact be too conservative in this scenario. Finally we observe that the material is evenly distributed along the length of the macroscopic structural members under axial load. In other words, the generated oriented microstructure is spatially regular and doesn't introduce undesirable perturbations or bottlenecks in the load paths.

6.8 De-homogenization of rank-2 laminates

Our method can also be applied to de-homogenize rank-2 laminate structures to obtain similar results compared to Elingaard et al. (2022). The pipeline of this previous work starts by generating patterns from a pre-trained convolutional neural network evaluating a branching loss, followed by a solidifying branching step (the reader is invited to refer

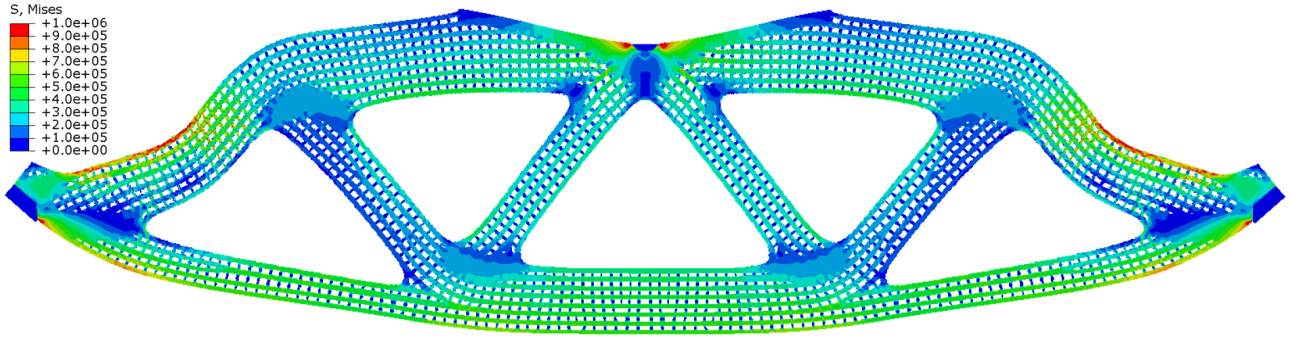

Figure 26: RD design variant of the MBB Beam at peak load in the non linear analysis color-coded by the von Mises stress.

h_c	μ_{min}	V_{ref}	h_f	ε_f	ε_i	Δx	$\mathcal{T}_i$	V_f	$T_{\{.\}}$[s]	Method
1/120	0.05	0.2532	$1/24h_c$	$60h_f$	$20h_i$	.	1920×960	0.2587	13.7	Elingaard et al. (2022)
					$7.5h_i$	2.9	720×360	0.2415	20.6	Ours
					$10h_i$	2.2	960×480	0.2473	23.7	Ours
					$20h_i$	1.1	1920×960	0.2449	61.8	Ours
1/120	0.10	0.2566	$1/24h_c$	$60h_f$	$20h_i$	.	1920×960	0.2586	13.7	Elingaard et al. (2022)
					$7.5h_i$	2.9	720×360	0.2524	22.6	Ours
					$10h_i$	2.2	960×480	0.2541	22.7	Ours
					$20h_i$	1.1	1920×960	0.2442	63.4	Ours
1/120	0.20	0.2572	$1/24h_c$	$60h_f$	$20h_i$	.	1920×960	0.2607	13.7	Elingaard et al. (2022)
					$7.5h_i$	2.9	720×360	0.2603	22.4	Ours
					$10h_i$	2.2	960×480	0.2639	23.3	Ours
					$20h_i$	1.1	1920×960	0.2609	71.3	Ours

Table 4: Comparison of the computational cost between Elingaard et al. (2022) method and ours for the de-homogenization of a 240×120 Michell cantilever input to a fine mesh of 5760×2880 elements with a wave-length of $\varepsilon_f = 60h_f$

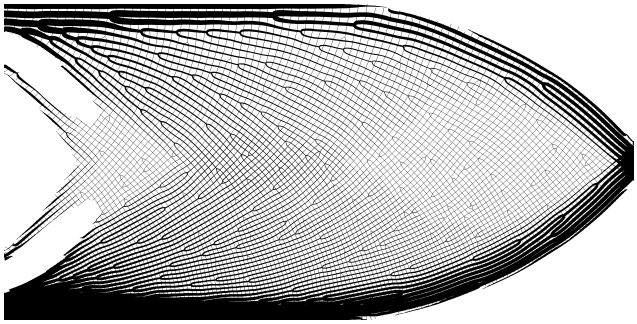

Figure 27: In this example the parameter γ is linearly increasing from the top ($\gamma = 0.5$) to the bottom ($\gamma = 2.5$) which has the effect to reduce the wave-length.

We also propose to compare the average computation time of the two methods by measuring the set {CNN forward + Loss eval. + Solidify branches + Upsampling} for Elingaard et al. (2022), and {Reaction/Diffusion $\mathcal{S}_1$ + $\mathcal{S}_2$ + Upsampling} for ours. In every example the initial state is composed of evenly spaced disk seeds uniformly distributed in the rectangular area ($20 \times 20\frac{n_x}{n_y}$ seeds of radius $0.015n_y$). The results are displayed in Table 4 for the de-homegenization of a 240×120 Michell cantilever input to a fine mesh of 5760×2880 elements with a wave-length of $\varepsilon_f = 60k_f$.

to their paper). In our case, we replaced these two first steps by the anisotropic Reaction/Diffusion growth. Then the density field s_i (generated with $\rho = 1$ and $\Gamma = 0$ everywhere) generated by R/D is plugged into the rest of Elingaard et al. (2022) pipeline, starting by the skeletonization step, in order to obtain the results shown in Fig. 28.

To validate that our method gives results as good as Elingaard et al. (2022) method, we provide a comparison of the performance of the two methods Table 5 for a set of 6 structures shown in Fig. 29 dehomogenized on a 2400×1200 mesh. We find that the values of $\frac{C_f \cdot V_f}{C_{ref} \cdot V_{ref}}$ - the ratio between the performance of the de-homogenized design and the reference solution (lower is better) - is close (sometimes higher, sometimes lower) to Elingaard et al. (2022) results.

An advantage of our Reaction/Diffusion-based approach is the possiblity to adapt the wavelength of the patterns in a flexible way without requiring a new training. This allows to generate structures with the same final wave-length using smaller sizes for the intermediate mesh thus decreasing the computation time of our method. While the computation cost of our method is higher, this disregards the 1-hour long training of a CNN which is only able to output a pattern of a fixed wavelength ε_i on the intermediate mesh. By varying spatially the parameter γ, it is even possible to obtain dehomogenized structures with a spatially variable wavelength as shown Fig. 27. Moreover one can note that our approach would also be valid in 3D without designing and training a new CNN architecture.

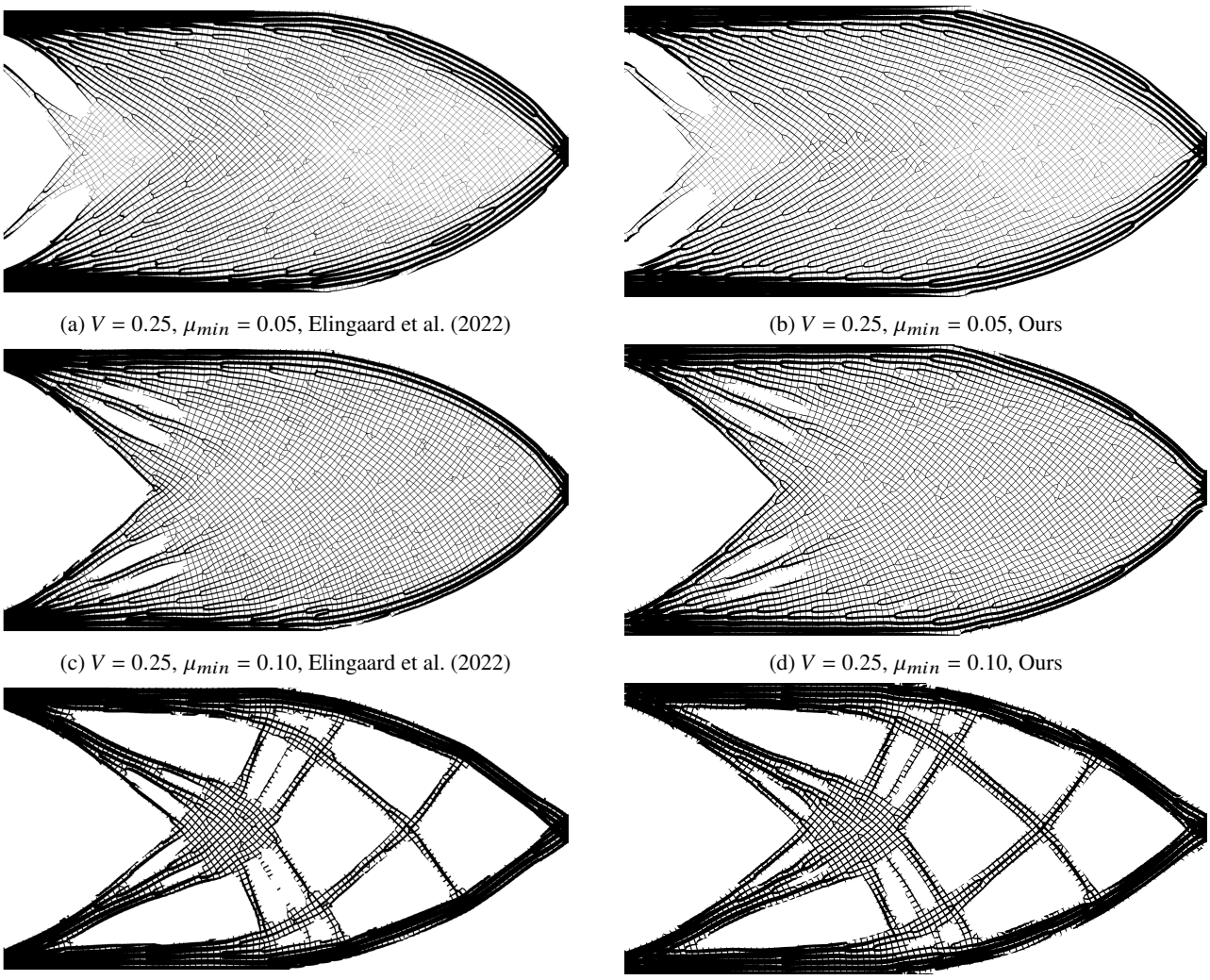

(a) $V = 0.25$, $\mu_{min} = 0.05$, Elingaard et al. (2022)

(b) $V = 0.25$, $\mu_{min} = 0.05$, Ours

(c) $V = 0.25$, $\mu_{min} = 0.10$, Elingaard et al. (2022)

(d) $V = 0.25$, $\mu_{min} = 0.10$, Ours

(e) $V = 0.25$, $\mu_{min} = 0.20$, Elingaard et al. (2022)

(f) $V = 0.25$, $\mu_{min} = 0.20$, Ours

Figure 28: De-homogenization of a 240×120 Michell cantilever input to a fine mesh of 5760×2880 elements with a wave-length of $\varepsilon_f = 60h_f$, with Elingaard et al. (2022) method (left) and our method (right). The figures generated with our method used an intermediate wave-length ε_i.

6.9 Manual Correction & Interactive Design

One of the main advantages of our method compared to others is its local aspect. As it is built upon a morphogenesis process it shows some biological properties such as adaptation and regeneration that one can efficiently use for structure design. For instance, the designer can interact with the structure by manually cutting, erasing or infilling some areas and let the reaction diffusion reacts to grow a different yet coherent new structure. Self-organization can be also used to combine different structures as shown Fig. 30. After having grown a structure for a specific scenario such as the multi-load bridge, the designer can decide to stick some existing structures previously generated (here these are the 3 owls) above. In order to compute the final structure there is no need to generate the entire structure from scratch. The designer can simply place the two objects in contact (a), with optional removal of material at the junction (b), and just let the structure grows from the existing parts (c). This technique can also lead to a fast generation of very high resolution shapes from precomputed parts.

Conclusion

The present work proposed a novel approach to design conforming lattice-like structures, inspired by morphogenesis. We developed a method relying on an anisotropic Reaction/Diffusion specific model, capable of growing patterns oriented by an underlying tensor field while remaining inside a prescribed 3D shape. By generating an oriented structure for each principal tensor direction taken independently, it is then possible to produce a global lattice-like shape by combination of these substructures with Boolean operations. Furthermore the thickness of the oriented pattern can be controlled by applying some filters before combining them.

Our method finds its application in the design of detailed lattice and membrane structures oriented by inputs which can be provided by a stress field or an anisotropic material orientation field inside a structurally optimized shape. In this context, our lattice-like structures come as a good trade-off between pure stiffness, stability or resistance to buckling. By non-linear numerical analysis we demonstrate that our optimized structure can support a buckling load approx-

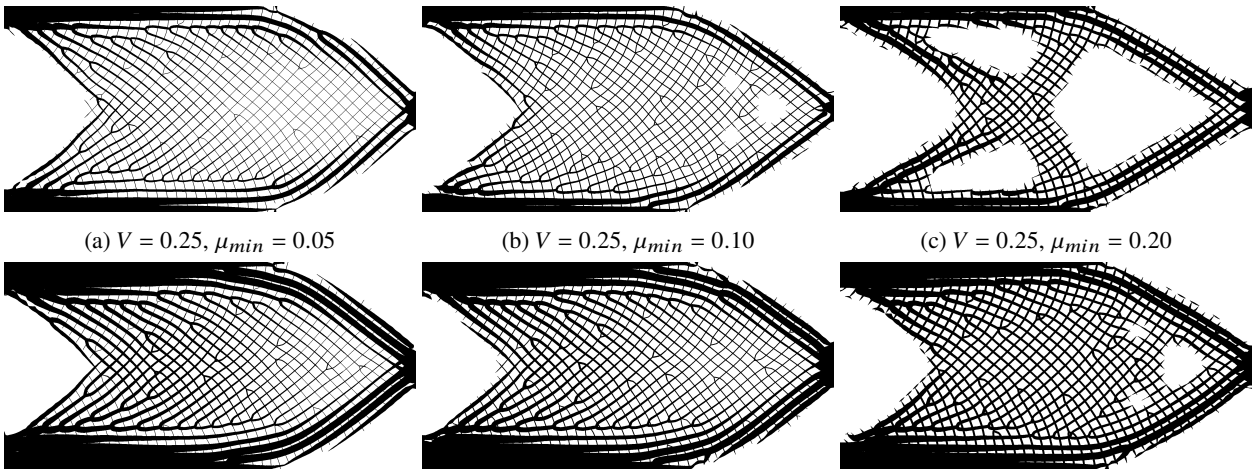

(a) $V = 0.25$, $\mu_{min} = 0.05$ (b) $V = 0.25$, $\mu_{min} = 0.10$ (c) $V = 0.25$, $\mu_{min} = 0.20$

(d) $V = 0.40$, $\mu_{min} = 0.05$ (e) $V = 0.40$, $\mu_{min} = 0.10$ (f) $V = 0.40$, $\mu_{min} = 0.20$

Figure 29: De-homogenization of a 60×30 Michell cantilever input to a fine mesh of 2400×1200 elements with a wave-length of $\varepsilon_f = 50h_f$ using our method.

h_c	ε_i	$\mathcal{T}_i$	μ_{min}	V_{ref}	C_{ref}	h_f	ε_f	V_f	C_f	$\frac{C_f \cdot V_f}{C_{ref} \cdot V_{ref}}$
Elingaard et al. (2022)										
1/30	$10h_i$	480×240	0.05	0.2535	106.21	$1/40h_c$	$50h_f$	0.2581	143.65	1.3770
1/30	$10h_i$	480×240	0.05	0.4024	68.58	$1/40h_c$	$50h_f$	0.4201	78.79	1.1993
1/30	$10h_i$	480×240	0.10	0.2568	113.61	$1/40h_c$	$50h_f$	0.2569	149.53	1.3167
1/30	$10h_i$	480×240	0.10	0.4080	69.00	$1/40h_c$	$50h_f$	0.4224	75.16	1.1279
1/30	$10h_i$	480×240	0.20	0.2614	122.86	$1/40h_c$	$50h_f$	0.2566	152.86	1.2214
1/30	$10h_i$	480×240	0.20	0.4165	73.37	$1/40h_c$	$50h_f$	0.4323	77.39	1.0949
Ours										
1/30	$12.5h_i$	600×300	0.05	0.2535	106.21	$1/40h_c$	$50h_f$	0.2570	135.46	1.2930
1/30	$12.5h_i$	600×300	0.05	0.4024	68.58	$1/40h_c$	$50h_f$	0.4281	78.17	1.2126
1/30	$12.5h_i$	600×300	0.10	0.2568	113.61	$1/40h_c$	$50h_f$	0.2667	156.12	1.4271
1/30	$12.5h_i$	600×300	0.10	0.4080	69.00	$1/40h_c$	$50h_f$	0.4332	81.16	1.2489
1/30	$12.5h_i$	600×300	0.20	0.2614	122.86	$1/40h_c$	$50h_f$	0.2808	134.78	1.1784
1/30	$12.5h_i$	600×300	0.20	0.4165	73.37	$1/40h_c$	$50h_f$	0.4432	75.22	1.0909

Table 5: Comparison of the performance between Elingaard et al. (2022) method and ours for the de-homogenization 60×30 Michell cantilever input to a fine mesh of 2400×1400 elements with a wave-length of $\varepsilon_f = 50h_f$

imately 70% higher than a classic topology optimization design without actually requiring an explicit modeling of buckling behavior.

The other main application of our approach is the de-homogenization of rank-2 laminates. Our results are comparable with state of the art methods such as (Elingaard et al., 2022) but our approach offers some key benefits. Specifically, we avoid the use machine learning approaches and the accompanying challenges of generating data, choosing a network architecture and training the network.

Due to its 2-scale nature, our method is fast and scalable to high resolution designs. Moreover, the microstructure generation is completely local, allowing the designer to dynamically interact with the growing structure, by erasing or modifying some parts and letting it evolve. Additionally, the aptitude of the Reaction/Diffusion to smoothly grow along the overall 3D shape ensure to generate structures with high lattice regularity, which is desirable both for aesthetics and mechanical performance.

Limitations & Future work

The substructures oriented independently by the tensor directions usually show great regularity thanks to the diffusion term but some defects can appear after the Boolean combination, at the boundary of the shape. Even if the Reaction/Diffusion can grow smoothly along the 3D shape, depending on the growing orientation, the pattern will not grow exactly at the exact same distance of the boundary, leading to damage artefacts after Boolean combination. Different methods could be investigated to overcome this problem, such as an explicit graph extraction using skeletonization or intersection points, or filtering constraints to enforce the Reaction/Diffusion to always grow at a constant distance of the boundary.

An explicit graph would also offer a lighter 3D representation as our method requires to work on high resolution grids when generating highly detailed shapes. For instance our optimized lattice chair necessitated to store more than 130M voxel values. In addition a graph representation would make it more compatible with CAD software as it constitutes an exact representation.

Empirical results show that our method reliably gener-

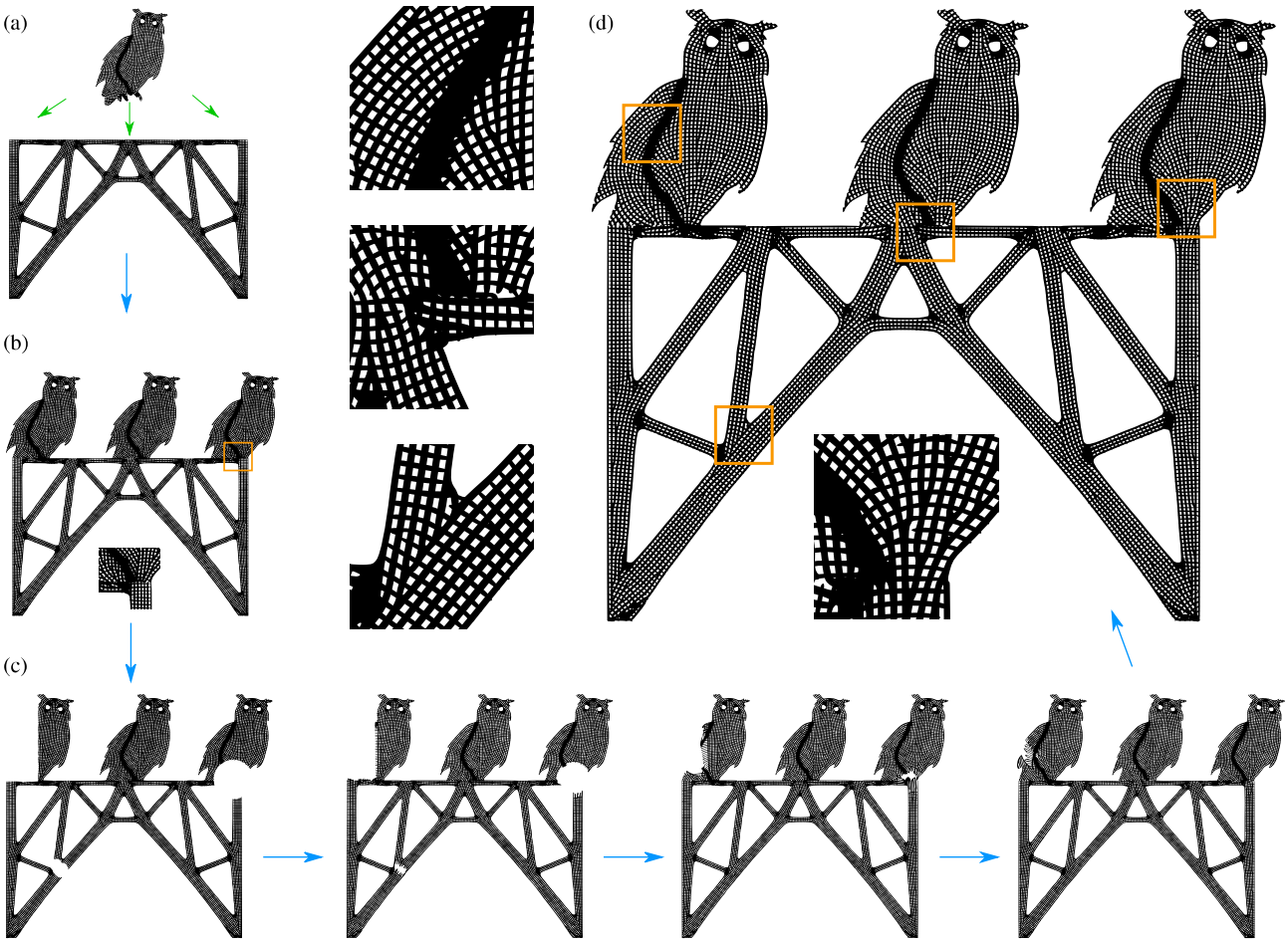

Figure 30: Combination of existing structures by self regeneration: (a) The owl structure is duplicated to be put on the bridge (b) The owl structures are concatenated to the bridge (c) Several damages are done in the structure which is then left to grow again to form the final whole structure (d)

ates efficient oriented infill patterns. However, it is worth noting that the Reaction-Diffusion process is not an optimization of an objective function so it does not guarantee to generate optimal results. In addition, the naive approach to completely infill problematic areas with fast orientation variations can waste some material from an optimization perspective. Unconnected patterns or topological defects can also lead to disconnected component near the boundary of the final structure.

Appendix

The stress tensor field can require additional regularization steps for being operable with our method. As we seek for a certain regularity in its associated rotation field $\mathbb{R}(\mathbf{x})$, this is not the case where the orientation is not clearly defined either because the stress is trivial ($\sigma_i \approx 0$) or because it is almost isotropic ($\sigma_i \approx \sigma_j$). In these regions the tensor can change almost randomly of directions from a neighbour to another which makes it difficult to build a regular structure. Hence we need to modify the tensor field in these areas such that the field becomes regular and in accordance with the other regions where the orientation of the stress field is well defined.

To this end, we start by setting to zeros the eigenvectors associated to not well-defined orientations i.e. where $|\sigma_i| < \sigma_{min}$ or $\big||\sigma_i| - |\sigma_j|\big| < \sigma_{min}$. Considering the other ones as well-defined we need to re-generate these trivial eigenvectors conformly to the other ones. In order to reduce the number of eigeinvectors to re-compute we make some simplifications: in the particular 2D case we set $\mathbf{v}_2(\mathbf{x}) = \mathbf{0}$ only if $\mathbf{v}_1(\mathbf{x}) = \mathbf{0}$ because only one vector is sufficient to describe the orientation so the second one suits if the first one does. In 3D we set $\mathbf{v}_3(\mathbf{x}) = \mathbf{0}$ only if $\mathbf{v}_2(\mathbf{x}) = \mathbf{0}$ for the same reason.

After this pre-treatment, two cases need to be considered in 3D. In 2D, for an element $\mathbf{x}$ considered it has either all its eigenvectors trivial or neither of them. That is not the case in 3D for which there is the case where the first one is non trivial and the two last ones are equal to zeros. As we aim to generate the trivial rotations as a mean of their non-zeros neighbours we need to have either $\mathbb{R}(\mathbf{x}) = 0$ or $\mathbb{R}(\mathbf{x}) = (\mathbf{v}_1(\mathbf{x}), \mathbf{v}_2(\mathbf{x}), \mathbf{v}_3(\mathbf{x}))$ with $\mathbf{v}_i(\mathbf{x}) \neq 0$. To this end we recompute the vectors $\mathbf{v}_2(\mathbf{x}) = \mathbf{v}_3(\mathbf{x}) = 0$ with non trivial first eigenvectors by selecting two non-colinear constant vectors $\mathbf{v}_\alpha$ and $\mathbf{v}_\beta$ which are likely to be not aligned with any of $\mathbf{v}_1(\mathbf{x})$ and we apply the simple algorithm 1.

Once we are brought back to the case where either the field $\mathbb{R}(\mathbf{x})$ is composed either of rotations or zeros, we can compute the missing rotations as a mean of their neighbours expressed in the same orthonormal basis following the algorithm 2. The function $closestMatrix(\mathbb{R}_a, \mathbb{R}_b)$ considers

Algorithm 1 : Complete the partially trivial orientations $\mathbb{R}(\mathbf{x})$

Let $\varepsilon \ll 1$
for $\mathbf{x} \in \Omega$ **do**
  if $\mathbf{v}_1(\mathbf{x}) \neq \mathbf{0}$ **and** $\mathbf{v}_2(\mathbf{x}) = \mathbf{0}$ **then**
    $\mathbf{v}_2(\mathbf{x}) = \mathbf{v}_1(\mathbf{x}) \times \mathbf{v}_\alpha$
    if $\|\mathbf{v}_2(\mathbf{x})\| < \varepsilon$ **then**
      $\mathbf{v}_2(\mathbf{x}) = \mathbf{v}_1(\mathbf{x}) \times \mathbf{v}_\beta$
    end if
    $\mathbf{v}_2(\mathbf{x}) \leftarrow \frac{\mathbf{v}_2(\mathbf{x})}{\|\mathbf{v}_2(\mathbf{x})\|}$
    $\mathbf{v}_3(\mathbf{x}) = \mathbf{v}_1(\mathbf{x}) \times \mathbf{v}_2(\mathbf{x})$
  end if
end for

the 8-symmetric group (in 2D) or the 48-symmetric group (in 3D) that expresses $\mathbb{R}_b$ in the $\mathbb{R}_a$ basis. After a sufficient number of steps every zeros-rotations should be replaced.

Algorithm 2 : Re-generate the trivial orientations $\mathbb{R}(\mathbf{x})$

Let $N(\mathbf{x})$ be the set of neighbours of $\mathbf{x}$ and $\mathbb{R}_{ref}$ the orientation matrix of the first neighbour $\mathbf{y} \in N(\mathbf{x})$ such that $\mathbb{R}(\mathbf{y}) \neq \mathbf{0}$.
for nStep **do**
  for $\mathbf{x} \in \Omega$ **do**
    if $\mathbb{R}(\mathbf{x}) = \mathbf{0}$ **then**
      for $\mathbf{y} \in N(\mathbf{x})$ **do**
        if $\mathbb{R}(\mathbf{y}) \neq \mathbf{0}$ **then**
          $\mathbb{R}_{tmp} = closestMatrix(\mathbb{R}_{ref}, \mathbb{R}(y))$
          $\mathbb{R}(\mathbf{x}) \leftarrow \mathbb{R}(\mathbf{x}) + \mathbb{R}_{tmp}$
        end if
      end for
      $\mathbb{R}(\mathbf{x}) \leftarrow Orthonormalize(\mathbb{R}(\mathbf{x}))$
    end if
  end for
end for

It should be noted that this second correction step is uncommon for structures designed by Topology Optimization as the optimization build the shape by following the load paths hence the stress should always be significant anywhere inside the structure.

Compliance with ethical standards

Conflict of Interest The authors declare that they have no conflict of interest.
Replication of Results Unless explicitly stated in the text, we used the following parameters: Young modulus = 1, Poisson Ratio = 0.3, $d = \frac{D_u}{D_v} = \frac{1}{2}$, $\gamma = 1$, $F = 0.0395$, $k = 0.0595$, $\alpha = 0.5$, $\xi = 5$.

References

Ahsan, A. M. M. N. and Khoda, B. (2021). Characterizing novel honeycomb infill pattern for additive manufacturing. Journal of Manufacturing Science and Engineering, 143(2):021002.

Alfaify, A., Saleh, M., Abdullah, F. M., and Al-Ahmari, A. M. (2020). Design for additive manufacturing: A systematic review. Sustainability, 12(19).

Allaire, G. and Aubry, S. (1999). On optimal microstructures for a plane shape optimization problem. Structural optimization, 17(2-3):86–94.

Allaire, G., Geoffroy-Donders, P., and Pantz, O. (2019). Topology optimization of modulated and oriented periodic microstructures by the homogenization method. Computers & Mathematics with Applications, 78(7):2197–2229.

Allaire, G. and Kohn, R. V. (1993). Optimal design for minimum weight and compliance in plane stress using extremal microstructures. European journal of mechanics. A. Solids, 12(6):839–878.

Andreassen, E., Clausen, A., Schevenels, M., Lazarov, B. S., and Sigmund, O. (2011). Efficient topology optimization in matlab using 88 lines of code. Structural and Multidisciplinary Optimization, 43(1):1–16.

Arora, R., Jacobson, A., Langlois, T. R., Huang, Y., Mueller, C., Matusik, W., Shamir, A., Singh, K., and Levin, D. I. (2019). Volumetric michell trusses for parametric design & fabrication. In Proceedings of the 3rd ACM Symposium on Computation Fabrication, SCF '19, New York, NY, USA. ACM.

Attene, M., Livesu, M., S. Lefebvre, T. F., Rusinkiewicz, S., Ellero, S., Martínez, J., and Bermano, A. H. (2018). Design, representations, and processing for additive manufacturing. Synthesis Lectures on Visual Computing: Computer Graphics, Animation, Computational Photography, and Imaging, 10(2):1–146.

Batischev, O. V., Batischeva, A. A., and Kholodov, A. S. (1999). Unstructured adaptive grid and grid-free methods for edge plasma fluid simulations. Journal of Plasma Physics, 61(5):701–722.

Bendsøe, M. P. (1989). Optimal shape design as a material distribution problem. Structural optimization, 1(4):193–202.

Bendsøe, M. P. and Kikuchi, N. (1988). Generating optimal topologies in structural design using a homogenization method. Computer methods in applied mechanics and engineering, 71(2):197–224.

Bendsøe, M. P. and Sigmund, O. (1999). Material interpolation schemes in topology optimization. Archive of applied mechanics, 69(9):635–654.

Bensoussan, A., Lions, J.-L., Papanicolaou, G., and Caughey, T. (1979). Asymptotic analysis of periodic structures. Journal of Applied Mechanics, 46(2):477.

Bommes, D., Zimmer, H., and Kobbelt, L. (2009). Mixed-integer quadrangulation. ACM Transactions On Graphics (TOG), 28(3):1–10.

Brennan-Craddock, J. (2011). The investigation of a method to generate conformal lattice structures for additive manufacturing. PhD thesis.

Chaturvedi, R., Huang, C., Kazmierczak, B., Schneider, T., Izaguirre, J. A., Glimm, T., Hentschel, H. G. E., Glazier, J., Newman, S., and Alber, M. (2005). On multiscale approaches to three-dimensional modelling of

morphogenesis. Journal of the Royal Society interface, 2(3):237–253.

Chi, M.-T., Liu, W.-C., and Hsu, S.-H. (2016). Image stylization using anisotropic reaction diffusion. Vis. Comput., 32(12):1549–1561.

Choi, J. S., Yamada, T., Izui, K., Nishiwaki, S., and Yoo, J. (2011). Topology optimization using a reaction–diffusion equation. Computer Methods in Applied Mechanics and Engineering, 200(29-32):2407–2420.

Clausen, A., Aage, N., and Sigmund, O. (2015). Topology optimization of coated structures and material interface problems. Computer Methods in Applied Mechanics and Engineering, 290:524–541.

Clausen, A., Aage, N., and Sigmund, O. (2016). Exploiting additive manufacturing infill in topology optimization for improved buckling load. Engineering, 2(2):250–257.

Dong, G., Tang, Y., and Zhao, Y. F. (2017). A survey of modeling of lattice structures fabricated by additive manufacturing. Journal of Mechanical Design, 139(10):100906.

Doursat, R., Sayama, H., and Michel, O. (2013). A review of morphogenetic engineering. Natural Computing, 12(4):517–535.

Du Plessis, A., Broeckhoven, C., Yadroitsava, I., Yadroitsev, I., Hands, C. H., Kunju, R., and Bhate, D. (2019). Beautiful and functional: a review of biomimetic design in additive manufacturing. Additive Manufacturing, 27:408–427.

Ebke, H.-C., Campen, M., Bommes, D., and Kobbelt, L. (2014). Level-of-detail quad meshing. ACM Transactions on Graphics (TOG), 33(6):1–11.

Elingaard, M. O., Aage, N., Bærentzen, J. A., and Sigmund, O. (2022). De-homogenization using convolutional neural networks. Computer Methods in Applied Mechanics and Engineering, 388:114197.

Emmendoerfer Jr, H. and Fancello, E. A. (2016). Topology optimization with local stress constraint based on level set evolution via reaction–diffusion. Computer Methods in Applied Mechanics and Engineering, 305:62–88.

FitzHugh, R. (1961). Impulses and physiological states in theoretical models of nerve membrane. Biophysical journal, 1(6):445–466.

Francfort, G. A. and Murat, F. (1986). Homogenization and optimal bounds in linear elasticity. Archive for Rational mechanics and Analysis, 94(4):307–334.

Fratzl, P. and Weinkamer, R. (2007). Nature's hierarchical materials. Progress in materials Science, 52(8):1263–1334.

Gao, X., Jakob, W., Tarini, M., and Panozzo, D. (2017). Robust hex-dominant mesh generation using field-guided polyhedral agglomeration. ACM Transactions on Graphics (TOG), 36(4):1–13.

Geoffroy-Donders, P., Allaire, G., and Pantz, O. (2020). 3-d topology optimization of modulated and oriented periodic microstructures by the homogenization method. Journal of Computational Physics, 401:108994.

Günter, S., Yu, Q., Krüger, J., and Lackner, K. (2005). Modelling of heat transport in magnetised plasmas using non-aligned coordinates. Journal of Computational Physics, 209(1):354–370.

GrabCAD (2013). Grabcad ge jet engine bracket challenge.

Gray, P. and Scott, S. (1984). Autocatalytic reaction in the isothermal continuous stirred tank reactor: Oscillations and instabilities in the system a + 2b $\rightarrow$ 3b; b $\rightarrow$ c. Chemical engineering science, 1:1087–1097.

Groen, J., Thomsen, C., and Sigmund, O. (2021). Multi-scale topology optimization for stiffness and de-homogenization using implicit geometry modeling. Structural and Multidisciplinary Optimization, pages 1–16.

Groen, J. P. and Sigmund, O. (2018). Homogenization-based topology optimization for high-resolution manufacturable microstructures. International Journal for Numerical Methods in Engineering, 113(8):1148–1163.

Groen, J. P., Stutz, F. C., Aage, N., Bærentzen, J. A., and Sigmund, O. (2020). De-homogenization of optimal multi-scale 3d topologies. Computer Methods in Applied Mechanics and Engineering, 364:112979.

Groen, J. P., Wu, J., and Sigmund, O. (2019). Homogenization-based stiffness optimization and projection of 2d coated structures with orthotropic infill. Computer Methods in Applied Mechanics and Engineering, 349:722–742.

Hagberg, A. and Meron, E. (1994). From labyrinthine patterns to spiral turbulence. Physical review letters, 72(15):2494.

Hutton, T., Munafo, R., Trevorrow, A., Rokicki, T., and Wills, D. (2015). Ready, a cross-platform implementation of various reaction-diffusion systems. https://github.com/GollyGang/ready.

Jakob, W., Tarini, M., Panozzo, D., and Sorkine-Hornung, O. (2015). Instant field-aligned meshes. ACM Trans. Graph., 34(6):189–1.

Kälberer, F., Nieser, M., and Polthier, K. (2007). Quadcover-surface parameterization using branched coverings. In Computer graphics forum, volume 26, pages 375–384. Wiley Online Library.

Kawasaki, K., Mochizuki, A., Matsushita, M., Umeda, T., and Shigesada, N. (1997). Modeling spatio-temporal patterns generated bybacillus subtilis. Journal of theoretical biology, 188(2):177–185.

Kim, T. and Lin, M. (2007). Stable advection-reaction-diffusion with arbitrary anisotropy. Comput. Animat. Virtual Worlds, 18(4–5):329–338.

Kindlmann, G., Weinstein, D., and Hart, D. (2000). Strategies for direct volume rendering of diffusion tensor fields. IEEE Transactions on Visualization and Computer Graphics, 6(2):124–138.

Kobayashi, R. (1993). Modeling and numerical simulations of dendritic crystal growth. Physica D: Nonlinear Phenomena, 63(3-4):410–423.

Kruiper, R., Chen-Burger, J., and Desmulliez, M. P. (2016). Computer-aided biomimetics. In Conference on Biomimetic and Biohybrid Systems, pages 131–143. Springer.

Kruiper, R., Vincent, J. F., Abraham, E., Soar, R. C., Konstas, I., Chen-Burger, J., and Desmulliez, M. P. (2018). Towards a design process for computer-aided biomimetics. Biomimetics, 3(3):14.

Lai, Y.-K., Kobbelt, L., and Hu, S.-M. (2008). An incremental approach to feature aligned quad dominant remeshing. In Proceedings of the 2008 ACM symposium on Solid and physical modeling, pages 137–145.

Lakes, R. (1993). Materials with structural hierarchy. Nature, 361(6412):511–515.

Liu, H., Hu, Y., Zhu, B., Matusik, W., and Sifakis, E. (2018a). Narrow-band topology optimization on a sparsely populated grid. ACM Transactions on Graphics (TOG), 37(6):1–14.

Liu, J., Gaynor, A. T., Chen, S., Kang, Z., Suresh, K., Takezawa, A., Li, L., Kato, J., Tang, J., Wang, C. C. L., Cheng, L., Liang, X., and To, A. (2018b). Current and future trends in topology optimization for additive manufacturing. Structural and Multidisciplinary Optimization, 57:2457–2483.

Lu, L., Sharf, A., Zhao, H., Wei, Y., Fan, Q., Chen, X., Savoye, Y., Tu, C., Cohen-Or, D., and Chen, B. (2014). Build-to-last: Strength to weight 3d printed objects. ACM Trans. Graph. (Proc. SIGGRAPH), 33(4):97:1–97:10.

Malheiros, M. d. G. and Walter, M. (2017). Pattern formation through minimalist biologically inspired cellular simulation. In Proceedings of the 43rd Graphics Interface Conference, GI '17, page 148–155, Waterloo, CAN. Canadian Human-Computer Communications Society.

Martínez, J., Dumas, J., and Lefebvre, S. (2016). Procedural voronoi foams for additive manufacturing. ACM Trans. Graph., 35(4).

Martínez, J., Song, H., Dumas, J., and Lefebvre, S. (2017). Orthotropic k-nearest foams for additive manufacturing. ACM Transactions on Graphics, 36(4):1–12.

Meier, E., Lukin, V., and Shumlak, U. (2010). Spectral element spatial discretization error in solving highly anisotropic heat conduction equation. Computer Physics Communications, 181(5):837–841.

Michell, A. (1904). Lviii. the limits of economy of material in frame-structures. Philosophical Magazine Series 1, 8:589–597.

Murray, J. D. (2001). Mathematical biology II: spatial models and biomedical applications, volume 3. Springer New York.

Nagumo, J., Arimoto, S., and Yoshizawa, S. (1962). An active pulse transmission line simulating nerve axon. Proceedings of the IRE, 50(10):2061–2070.

Nguyen, J., in Park, S., Rosen, D., Folgar, L., and Williams, J. (2012). Conformal lattice structure design and fabrication. Solid Freeform Fabrication Symposium, Austin, TX, pages 138–161.

Pantz, O. and Trabelsi, K. (2008). A post-treatment of the homogenization method for shape optimization. SIAM Journal on Control and Optimization, 47(3):1380–1398.

Pearson, J. A. (1993). Complex patterns in a simple system. Science, 261:189–192.

Pedersen, P. (1989). On optimal orientation of orthotropic materials. Structural optimization, 1:101–106.

Pedersen, P. (2000). On optimal shapes in materials and structures. Structural and multidisciplinary optimization, 19(3):169–182.

Podersen, P. (1998). Some general optimal design results using anisotropic, power law nonlinear elasticity. Structural optimization, 15(2):73–80.

Podroužek, J., Marcon, M., Ninčević, K., and Wan-Wendner, R. (2019). Bio-inspired 3d infill patterns for additive manufacturing and structural applications. Materials, 12(3):499.

Pérez-Grande, D., Gonzalez-Martinez, O., Fajardo, P., and Ahedo, E. (2016). Analysis of the numerical diffusion in anisotropic mediums: Benchmarks for magnetic field aligned meshes in space propulsion simulations. Applied Sciences, 6(11).

Sanal, R. (2014). Numerical simulation of dendritic crystal growth using phase field method and investigating the effects of different physical parameter on the growth of the dendrite. arXiv preprint arXiv:1412.3197.

Sanderson, A., Kirby, R., Johnson, C., and Yang, L. (2006). Advanced reaction-diffusion models for texture synthesis. Journal of Graphics Tools, 11:47 – 71.

Sanderson, A. R., Johnson, C. R., and Kirby, R. M. (2004). Display of vector fields using a reaction-diffusion model. In Proceedings of the Conference on Visualization '04, VIS '04, page 115–122, USA. IEEE Computer Society.

Schmidt, M.-P., Couret, L., Gout, C., and Pedersen, C. (2020). Structural topology optimization with smoothly varying fiber orientations. Structural and Multidisciplinary Optimization, 62.

Schmidt, M.-P., Pedersen, C. B., and Gout, C. (2019). On structural topology optimization using graded porosity control. Structural and Multidisciplinary Optimization, 60(4):1437–1453.

Sigmund, O. (1997). On the Design of Compliant Mechanisms Using Topology Optimization. Mechanics of Structures and Machines, 25(4):493–524. Publisher: Taylor & Francis.

Sigmund, O. (2001). A 99 line topology optimization code written in matlab. Structural and multidisciplinary optimization, 21(2):120–127.

Soler, J., Schwander, F., Giorgiani, G., Liandrat, J., Tamain, P., and Serre, E. (2020). A new conservative finite-difference scheme for anisotropic elliptic problems in bounded domain. Journal of Computational Physics, 405:109093.

Stutz, F., Groen, J., Sigmund, O., and Baerentzen, J. (2020). Singularity aware de-homogenization for high-resolution topology optimized structures. Structural and Multidisciplinary Optimization, 62(5):2279–2295.

Stutz, F. C., Olsen, T. F., Groen, J. P., Trung, T. N., Aage, N., Sigmund, O., Solomon, J., and Bærentzen, J. A. (2022). Synthesis of frame field-aligned multi-laminar structures. ACM Trans. Graph. Just Accepted.

Svanberg, K. (1987). The method of moving asymptotes - a new method for structural optimization. International Journal for Numerical Methods in Engineering, 24(2):359–373.

Tang, M. and Wang, Y. (2017). An asymptotic preserving method for strongly anisotropic diffusion equations based on field line integration. Journal of Computational Physics, 330:735–748.

Tricard, T., Tavernier, V., Zanni, C., Martínez, J., Hugron, P.-A., Neyret, F., and Lefebvre, S. (2020). Freely orientable microstructures for designing deformable 3d prints. ACM Trans. Graph., 39(6).

Turing, A. M. (1952). The chemical basis of morphogenesis. Philosophical Transactions of the Royal Society of London. Series B, Biological Sciences, 237(641):37–72.

Umansky, M. V., Day, M. S., and Rognlien, T. D. (2005). On numerical solution of strongly anisotropic diffusion equation on misaligned grids. Numerical Heat Transfer, Part B: Fundamentals, 47(6):533–554.

van Es, B., Koren, B., and de Blank, H. J. (2016). Finite-volume scheme for anisotropic diffusion. Journal of Computational Physics, 306:422–442.

Witkin, A. and Kass, M. (1991). Reaction-diffusion textures. SIGGRAPH Comput. Graph., 25(4):299–308.

Wood, L. W. (1960). Relation of strength of wood to duration of load. U.S. Dept. of Agriculture, Forest Service, Forest Products Laboratory Report.

Wu, J., Aage, N., Westermann, R., and Sigmund, O. (2018). Infill optimization for additive manufacturing—approaching bone-like porous structures. IEEE Transactions on Visualization and Computer Graphics, 24(2):1127–1140.

Wu, J., Clausen, A., and Sigmund, O. (2017). Minimum compliance topology optimization of shell–infill composites for additive manufacturing. Computer Methods in Applied Mechanics and Engineering, 326:358–375.

Wu, J., Sigmund, O., and Groen, J. P. (2021a). Topology optimization of multi-scale structures: A review. Structural and Multidisciplinary Optimization, 63:1455–1480.

Wu, J., Wang, W., and Gao, X. (2021b). Design and optimization of conforming lattice structures. IEEE transactions on visualization and computer graphics, 27(1):43–56.

Yamada, T., Izui, K., Nishiwaki, S., and Takezawa, A. (2010). A topology optimization method based on the level set method incorporating a fictitious interface energy. Computer Methods in Applied Mechanics and Engineering, 199(45-48):2876–2891.

Yang, T. and Wang, Y. (2019). A new tailored finite point method for strongly anisotropic diffusion equation on misaligned grids. Applied Mathematics and Computation, 355:85–95.

Zhang, Y., Wang, Z., Zhang, Y., Gomes, S., and Bernard, A. (2020). Bio-inspired generative design for support structure generation and optimization in additive manufacturing (am). CIRP Annals, 69(1):117–120.

Zhou, Y., Lohan, D. J., Zhou, F., Nomura, T., and Dede, E. M. (2022). Inverse design of microreactor flow fields through anisotropic porous media optimization and dehomogenization. Chemical Engineering Journal, 435:134587.